



**Microscopic dynamics in room-temperature ionic liquids
confined in materials for supercapacitor applications**

Journal:	<i>Sustainable Energy & Fuels</i>
Manuscript ID	SE-REV-09-2019-000829.R1
Article Type:	Review Article
Date Submitted by the Author:	11-Sep-2019
Complete List of Authors:	Osti, Naresh; Oak Ridge National Laboratory Mamontov, Eugene; Oak Ridge National Laboratory, Spallation Neutron Source

ARTICLE

Microscopic dynamics in room-temperature ionic liquids confined in materials for supercapacitor applications

Naresh C. Osti*^a and Eugene Mamontov*^a

Received 00th January 20xx,
Accepted 00th January 20xx

DOI: 10.1039/x0xx00000x

Performance of electrical double layer capacitors (EDLCs), also known as supercapacitors, which are composed of porous electrodes and ionic liquid electrolytes, depends largely on the structure and dynamics of molecules/ions on the electrode-electrolyte interfaces. Immobilization of ions on electrodes surface and diffusivity of ions in the middle of the pores are two important phenomena influencing performance of supercapacitors. In recent years, porous carbon or metal carbide derived electrodes and ionic liquids electrolytes, either in the neat state, or mixed with organic solvents, were used to improve the energy and power density of supercapacitors. The molecular/ionic level predictive understanding of ions immobilization and movement inside the pores can be achieved, in principle, using molecular dynamics (MD) simulations. This calls for experimental techniques capable of validating MD predictions and providing directions for the future MD studies. Neutron scattering techniques, particularly quasi-elastic neutron scattering (QENS), uniquely provide information directly comparable with MD simulations results. This includes electrolytes confined in the electrode materials, due to high penetrative power of neutrons and their high sensitivity to hydrogen-bearing species. This paper reviews recent research where QENS, together with electrochemical measurements and molecular dynamics simulations, have been employed to explore the complex electrode/electrolyte systems, which is critical for developing predictive understanding of the charge storage mechanism in supercapacitors.

Introduction

To address the energy needs of today and tomorrow, electrical energy storage technologies have attracted much attention from the research community. Various energy storage technologies¹⁻³ have been explored after the invention of battery in 1800 by Alessandro Volta. Most of the early days efforts on batteries were invested in producing batteries with more steady current that could be recharged.⁴⁻⁶ Those efforts have resulted in many different types of batteries that can power up various electrical devices for a long period of time. However, because of the required safe charging rate associated with a battery, it takes a long time for the battery to fully charge once it becomes discharged. This slow charging rate, which is quite unavoidable in batteries, calls for an alternative energy storage technology that can override the present power limitations, especially for high-power applications.⁷⁻⁹ In this regard, electrochemical capacitors, also called electrical double layer capacitors (EDLCs), have been on the forefront of active research lately.^{7, 10-13} EDLCs consist of an electrolyte and electrodes, where charges are stored on the solid (electrodes)-electrolyte interface (SEI), electrostatically, as illustrated in Fig. 1.¹³ They deliver high power density, have a long lifetime, and can be charged within a short time.¹⁴ SEI of EDLCs can be tuned to enhance the device performances. Energy and the power density of supercapacitors are directly related to the materials used, more specifically, the electrodes and the electrolytes.^{12, 15-18} The physico-chemical interactions between the electrode

surfaces and the electrolyte molecules are a key to control the electro-chemical performance of supercapacitors. Structure and dynamics of fluids at SEI differ significantly from their respective bulk properties. Various electrodes (such as pure carbon and its allotropes) and electrolytes (aqueous, organic and ionic liquids) have been tested as supercapacitor materials. Most recent studies involved porous carbon as matrices and room temperature ionic liquids (RTILs) as electrolytes. The high surface area of porous carbon^{19, 20} and the wider operational voltage window of ionic liquids^{14, 21, 22} make them the materials

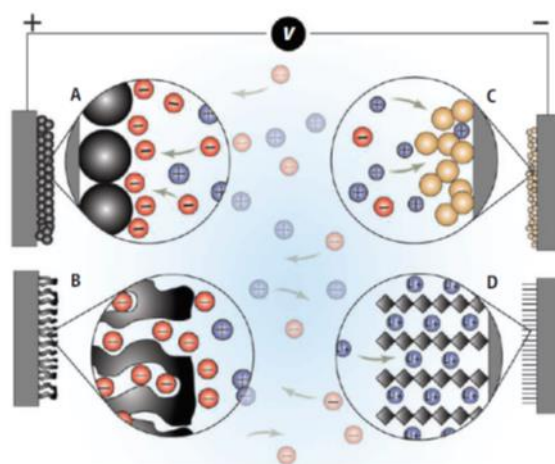


Fig. 1. Schematic representation of charge storage by EDLCs from adsorption of electrolyte ions on the surface of the electrodes. Formation of double layers on (a) carbon particle and (b) porous carbon surfaces is presented. Panels (c) and (d) show a mechanism of double layer formation and ion intercalation, respectively. From P. Simon *et al.*, *Science*, 2014, 343, 1210-1211. Reprinted with permission from AAAS.

^a Neutron Scattering Division, Oak Ridge National Laboratory, Oak Ridge, TN 37830, USA. Email: ostinc@ornl.gov and mamontove@ornl.gov

of choice for supercapacitors. Besides, other intrinsic properties of those materials, such as surface chemistries and typical pore sizes, along with the viscosity, diffusivity, and conductivity of ionic liquids provide added advantages for their use in device applications.

Understanding the structure, together with the microscopic dynamics of ions at the SEI, is essential for a rational design of energy storage devices. More specifically, mobility of electrolytes at the SEIs is associated with the performance of supercapacitors. Molecular level information on SEI properties may facilitate fine tuning the structure of the materials at the atomic level to enhance the device efficiency. The existing literature is rich with publications where a number of experimental techniques, such as nuclear magnetic resonance (NMR), electrochemical quartz crystal microbalance, electrochemical impedance spectroscopy, and small angle scattering²³⁻²⁵ have been employed to study the structure of SEI formed in supercapacitors. Those findings are extensively discussed in various reviews.^{14, 26-28} The length scale probed in an experiment is technique-specific; for example, pulsed-field gradient NMR measures diffusion on the length scales on the range of 100 nm to about 100 μm . Lacking to date is a review of experimental studies investigating the physico-chemical mechanisms on the nanometer length scale that underlie the electrochemical performance, specifically, microscopic dynamics of room-temperature ionic liquids confined in supercapacitor materials, although reviews of computer simulation studies of confined RTILs are available.^{29, 30} Among the experimental techniques, quasielastic neutron scattering (QENS) is arguably the only method (and the only technique in general, besides molecular dynamics simulations) suitable for measurements of the ion diffusivity parameters, such as diffusion jump rate and length, on the atomic and nanometer length scale. Importantly, due to high penetrative power of neutrons and their high sensitivity to hydrogen-bearing species, QENS can readily probe electrolyte mobility inside the electrode material. There are quite a few studies where QENS has been employed to resolve the microscopic dynamics and ions immobilization in different types of ionic liquids confined in electrode materials of various shape, size, and morphologies. The main objective of the present review is to summarize the contribution of QENS to the fundamental understanding of ionic liquids dynamics in supercapacitor materials. This may be broadly beneficial to researchers working on energy storage, by helping them to understand the underlying physics and chemistry aspects of supercapacitor devices. Our approach is to briefly introduce the EDLCs, summarizing their advantages and limitations, with an emphasis on the systems comprising an ionic liquid as an electrolyte and a carbon-based material as an electrode. Then, following a basic description of practical aspects of QENS, the capabilities of this technique to measure microscopic dynamics of various ionic liquids, in bulk state and confined in carbon-based media, are reviewed.

Electrical Double Layer Capacitors (EDLCs)

The growing need for energy consumption has generated strong interest in exploring and inventing better energy storage

and release technologies. Depletion of the fossil fuels have led to a higher demand for renewable sources, such as solar and wind. However, the intermittent nature of those sources necessitates the devices that can store energy and release it on demand for future use. Consequently, energy storing technologies, especially EDLCs, have attracted much attention nowadays. The increasing interest in EDLCs is due to the remarkably high energy but low power density associated with the conventional batteries, making charging them a lengthy process.^{4, 31} EDLCs, on the other hand, provide a high power density compared to batteries, but still suffer from a low energy density, along with a relatively high production cost.^{14, 32} There have been continuous efforts to increase the energy density and lower the production cost of the supercapacitors after they were introduced to public in 1957. Those efforts rely on the fundamental understanding of the working principle of the supercapacitors.

Capacitance (c), an ability of a device to store charge on electrodes by electrostatic adsorption of ions from electrolytes, is given by:¹⁴

$$c = \frac{\epsilon_e \epsilon_0 A}{d} \quad (1)$$

where ϵ_e and ϵ_0 represent the dielectric constants of the electrolytes and that of vacuum, respectively. The parameter d describes the thickness of the electric double layer formed on the electrodes having specific surface area (SSA), A . Quantitatively, the energy stored (E) in EDLCs is expressed as:¹⁴

$$E = \frac{CV^2}{2} \quad (2)$$

where V is the voltage between the electrodes. From the equations (1) and (2), it is evident that the energy stored in EDLCs is primarily controlled by the SSA of the electrodes and the applied voltage, V , which is limited by the stability window of the electrolytes used. In this regard, improving the electrodes (especially via increasing the surface area) and employing the electrolytes of high stability for a broad range of applied potentials should lead to higher performance. Various electrode materials of diverse morphologies have been tested in supercapacitors configurations using organic, inorganic, and ionic liquids as electrolytes. With a goal of increasing the SSA, activated carbons have been employed.^{18, 19, 33} This approach not only maximizes the charge adsorption area, but also lowers the production expenses of the EDLCs because of the relatively lower purchasing cost of carbon.^{19, 34} Extreme treatments (such as high temperatures and strong acids) of carbon-containing precursors during synthesis predominantly control the shape and size of the carbon pores. An overview of porous carbon synthesis and characterization is beyond the scope of this review, as more details about the EDLCs electrode materials are found elsewhere.³⁵⁻³⁷

The use of porous carbon electrodes has significantly increased the gravimetric capacitance compared to its bulk counterparts.³⁸ The interplay between the pore size and the electrolyte ions size has a major impact on the capacitance of the EDLCs. In order to achieve a higher capacitance, variation of the electrolytes is a common approach. Almost a two-fold increase in the capacitance has been reported when an organic

electrolyte is replaced by an aqueous electrolyte.^{39, 40} The energy and power density of EDLCs can also be improved by increasing the applied potential. However, stability window (i.e., the voltage above which breaking down of the electrolyte starts) is another factor which needs to be considered. An aqueous electrolyte starts to dissociate above 1 V of applied potential,¹⁴ whereas organic electrolytes can withstand higher voltage, but have high vapor pressure and are flammable, making their use a safety challenge. To overcome these limitations, room temperature ionic liquids (RTILs) have been used as electrolytes in supercapacitors.^{41, 42} RTILs have low vapor pressure, are solvent free, and are stable over a wide temperature and voltage window.⁴³ Therefore, supercapacitors featuring RTILs as electrolytes and porous carbon as electrodes have been explored in the last decade. It is certain that the interface between the RTILs and the surface of the porous carbon electrodes plays various important roles in controlling the electrochemical performances of supercapacitors. Therefore, a detailed molecular level understanding of the SEI comprised of RTILs in confined porous carbon matrices is of eminent importance.

Exploring the structure and dynamics at electrolyte-electrode interfaces in supercapacitors requires implementation of a wide array of techniques that can provide the pertinent information at various length scales, including molecular-level information at the nano scale. Since electrolyte/electrode interfaces are complex by their nature, there are few experimental techniques that can facilitate molecular level understanding of the interfaces. Furthermore, the interfaces change significantly during charging and discharging, which adds another level of complexity to their characterization, i. e., *in-situ* capability requirements to the instrumentation methods, which are not available with most of the instruments that can probe interfaces.

There are several experimental techniques that can characterize the fluid-solid interfaces. X-ray photoelectron spectroscopy (XPS) and Fourier transform infrared (FTIR) spectroscopy have been used to investigate the chemical modifications of the SEI. It should be noted that high vacuum required for application of surface-sensitive techniques, such as XPS, is often associated with a modification of the surface probed. XPS explores the interface of 5 nm or smaller thickness and provides chemical compositions as well as valence states of the chemical species present,⁴⁴ but, to investigate bulkier interface comprised of solid (electrode) and liquid (electrolyte), FTIR⁴⁵ has been employed. Besides these techniques, nuclear magnetic resonance has also been extensively used⁴⁶⁻⁴⁸ to resolve the structure and dynamics of the interfaces in working electrodes in real time. Because of the elemental selectivity, this technique probes structure evolution together with the mobility of chemical species such as ions, electrolytes, and solvent molecules at the interface, while the system is in operational configurations. Dynamics studies involving NMR provide the time scale of the motion of those chemical species, but not the nano-scale spatial information regarding this motion. From the computational side, classical density functional theory (cDFT)^{29, 49, 50} has been extensively applied to predict the SEI structure of the RTILs and porous carbon. On the other hand, to obtain both the temporal and the spatial information, molecular dynamics (MD) simulations^{51, 52} have been widely used to investigate the SEI comprising RTILs and porous carbon, from which translational diffusivities along with

the diffusion jump rate and length can be derived. Quasielastic neutron scattering is the only experimental technique that explores simultaneously the structure and dynamics at nano scales. QENS has been extensively used to investigate the dynamics of various RTILs in bulk state, but the use of QENS to explore the interfaces of RTILs and porous carbon has been attempted only recently. There are several RTILs and porous carbon confining systems where QENS has revealed the mechanisms by which ions become adsorbed on the surfaces of the electrodes, thereby altering the device electrochemical performance. To interpret the results of such QENS studies, it is helpful to have a basic understanding of this technique's capabilities and limitations.

Quasielastic neutron scattering as a probe of microscopic dynamics

Neutron is a neutral sub-atomic particle of half spin with a magnetic moment that exhibits a wave-mechanical duality. Kinetic energy and wave vector are associated with a neutron. Depending on the production sources, neutrons may have variable energies and wavelengths. The energy associated with "cold" neutrons (less than ca. 25 meV) is on the order of intermolecular energies, and the corresponding wavevector is on the order of molecular dimensions. These properties of neutrons make them a powerful tool to investigate the structure and dynamics of materials in neutron scattering experiments. Neutron scattering is exceptionally sensitive to hydrogen because of hydrogen's high incoherent neutron scattering cross-section. The total scattering cross-section of natural H is 82.02 barn for 25 meV neutrons (1 barn = 10^{-28} m²), with the incoherent cross-section accounting for 80.26 barn. The total scattering cross-sections of most other elements are in the range of a few barn. The high incoherent scattering cross-section of hydrogen makes diffraction studies of hydrogen-bearing systems problematic, unless substitution with deuterium is performed. On the other hand, it makes neutron scattering a powerful probe to resolve microscopic dynamics of hydrogen-bearing species, such as ionic liquids in bulk and in confinement. While all the elements in the sample contribute to the neutron scattering signal, for a typical hydrogen-bearing compound more than 90 % of neutrons are scattered by its hydrogen atoms. For a chemical confined in a carbon- or oxide-based matrix, the total scattering from the matrix may even dominate the signal in some cases, depending on the relative volume filled with the hydrogen-bearing material, yet in most cases the contribution from the confined chemical remains significant, and its microscopic dynamics can be analyzed.

The QENS technique has been successfully employed to probe microscopic dynamics in bulk and confined water,⁵³ as well as in polymers,⁵⁴⁻⁵⁷ biopolymer⁵⁸ and hard condensed matter.^{59, 60} In a typical QENS experiment, one measures the amount of energy and momentum transferred between the neutron and the scattering species. A change in the energy of neutrons provides a time scale of the atomic dynamics of the probed system, whereas the momentum transfer, which can be related to the scattering angle, provides the length scale information. Hence, QENS is a technique to probe both the diffusivity and diffusion mechanism at an atomic/molecular level. Since most elements have both coherent and incoherent neutron scattering cross-sections, the measured QENS intensity has a contribution from both types of scattering events. Double

differential scattering cross-section, which is measured during the scattering process, is given by:⁶¹

$$\frac{\partial^2 \sigma}{\partial \Omega \partial E} = \left(\frac{\partial^2 \sigma}{\partial \Omega \partial E} \right)_{incoh} + \left(\frac{\partial^2 \sigma}{\partial \Omega \partial E} \right)_{coh} \quad (3)$$

where σ is the scattering cross-section of the elements, Ω is the solid angle, and E is the energy transfer of neutron, $E = \hbar\omega$. The first term on the right side of equation (3) is the contribution from incoherent scattering, which depends on the individual atomic nuclei and represents the single-particle dynamics of the scattering species. The second term on the right side of equation (3) is the coherent contribution, which represents the collective motions of the atoms/molecules in a sample. When hydrogen atoms (which has a very high incoherent scattering cross-section) are present in the sample, the coherent contribution oftentimes becomes relatively small and usually can be neglected, except at the momentum transfers corresponding to the strong structural peaks. Therefore, we only focus on the incoherent part of the double differential scattering cross-section, which is related to the individual particle's incoherent scattering cross-section, σ_{incoh} , and dynamic structure factor, $S_{incoh}(Q, E)$, as:⁶¹

$$\begin{aligned} \frac{\partial^2 \sigma}{\partial \Omega \partial E} &= \left(\frac{\partial^2 \sigma}{\partial \Omega \partial E} \right)_{incoh} \\ &= \frac{1}{4\pi N} \frac{|\vec{k}_f|}{|\vec{k}_i|} [\sigma_{incoh} S_{incoh}(Q, E)] \end{aligned} \quad (4)$$

Here, N is the total number of scattering centers, k_f and k_i are the magnitude of the final and initial wave vectors of the neutron, and the momentum transfer $Q = |\vec{Q}| = |\vec{k}_i - \vec{k}_f|$. $S_{incoh}(Q, E)$ is the incoherent dynamic structure factor that has the information on the single-particle dynamic processes in a sample. It is also a time-Fourier transformation of the intermediate scattering function, $I(Q, t)$, which, upon additional space-Fourier transformation, gives the single-particle auto correlation function, $G(r, t)$. The decay of the $I(Q, t)$ with time (particularly, at $t = \infty$) suggests the types of atomic or molecular motions (long-range translational diffusion, or local) of the particles in the system. In the case of long-range translational diffusion, the $I(Q, t)$ decays to zero at $t = \infty$, whereas for localized motion, the $I(Q, t)$ plateaus at a finite value at $t = \infty$. Therefore, a possibility to directly compare the intermediate scattering function, or the auto correlation function calculated from the molecular dynamic simulations, with the QENS data further attests to the usefulness of this technique. QENS experiments can be performed using backscattering or time-of-flight (TOF) spectrometers. Backscattering spectrometers use crystal analyzers to select the neutron final energy, whereas the initial neutron energy is determined by some other means. These spectrometers built at neutron reactors provide sub- μeV resolution with somewhat limited dynamic range of accessible energy (ca. $\pm 30\text{-}35 \mu\text{eV}$). When built at spallation neutron sources, such spectrometers feature somewhat coarser energy resolution (down to a few μeV), but a much wider range of accessible energy transfers of hundreds of μeV . TOF spectrometers use either a system of choppers or a monochromator to select the initial neutron energy, whereas the neutron final energy is determined from its time-of-flight. TOF spectrometers are versatile and allow easy tradeoff between the energy resolution and intensity, but generally feature coarser energy resolution compared to their backscattering counterparts.

In many QENS experiments, the measured scattering intensity, $S(Q, E)$, can be analyzed using an empirical expression:⁶¹

$$S(Q, E) = [x(Q)\delta(E) + (1 - x(Q))S_{incoh}(Q, E)] \otimes R(Q, E) + B(Q, E) \quad (5)$$

The elastic scattering contribution weight, $x(Q)$, accounts for the fraction of particles immobile on the time scale defined by the spectrometer resolution and can be zero in experiments on liquids whose diffusion mobility can be fully resolved. $\delta(E)$ is the Dirac delta function, accounting for the completely elastic scattering events. $R(Q, E)$ is the instrument resolution, often measured from the very same sample at a low temperature ($\leq 20 \text{ K}$), where all diffusion mobility has ceased. $B(Q, E)$ is a background term that accounts, besides the measurement backgrounds, for the motions much faster than the motions which can be probed with a given spectrometer. In a typical approach, when QENS spectra are analyzed to determine $S_{incoh}(Q, E)$ at each Q value independently and then the Q dependence of the resulting $S_{incoh}(Q, E)$ is analyzed, the $x(Q)$ is a fitted parameter and $B(Q, E)$ is a fitted function (usually, but not always, linear in E , or a constant). Very recently, QENS data for a bulk RTIL (for which $x(Q)=0$) have been successfully analyzed using simultaneous fitting at all Q values with a "global" $S_{incoh}(Q, E)$.⁶² $S_{incoh}(Q, E)$ will be referred to hereon out as $S_{QE}(Q, E)$ because in QENS inelastic peaks are not observed together with a quasielastic signal due to the limited dynamic range accessible to the instrument. $S_{QE}(Q, E)$ appears as a broadening of a scattering signal over the elastic peak, called quasi-elastic (QE) broadening. While width of QE broadening represents the time scale of particle motion measured in the sample, the shape of the peak reflects the character of the respective dynamic process. The $S_{QE}(Q, E)$ for a long-range translational motion (mostly in liquids) is a simple Lorentzian function. For the localized motion (such as diffusion in confinement), an additional delta function term is present in the $S_{QE}(Q, E)$. However, when the system becomes more complex, a more complex model scattering function may be required. Often, though not always, $S_{QE}(Q, E)$ can be modeled to either a single Lorentzian function, or a sum of two Lorentzian functions, as⁶³

$$\begin{aligned} S_{QE}(Q, E) &= p_{narrow}(Q) \frac{1}{\pi} \frac{\Gamma_{narrow}(Q)}{\Gamma_{narrow}^2(Q) + E^2} \\ &+ (1 - p_{narrow}(Q)) \frac{1}{\pi} \frac{\Gamma_{broad}(Q)}{\Gamma_{broad}^2(Q) + E^2} \end{aligned} \quad (6)$$

In equation (6), $\Gamma_{narrow}(Q)$, and $\Gamma_{broad}(Q)$ are the half width at half maximum (HWHM) of two Lorentzians with their corresponding spectral weights of $p_{narrow}(Q)$ and $(1 - p_{narrow}(Q))$ respectively. The narrow and broad Lorentzian functions correspond to the slower and faster dynamic components in the system. The distinct dynamic components are not always directly associated with distinct populations of species of variable mobility. Depending on the measured E and Q range, the same molecular species could give rise, e.g., to the faster dynamic component due to the localized motion and slower dynamic component due to the long-range translation diffusion. The Q -dependence of the HWHMs is used to characterize the nature of the diffusion processes that give rise to the QE broadening.

In more complex systems, QE broadenings may deviate from Lorentzian shape. In those cases, $S_{QE}(Q, E)$ can be modeled to

a more complicated functional forms, such as Cole-Cole distribution⁶⁴ or Fourier transformed stretched exponential functions.⁶⁵ Both of those functions have one extra parameter, called a stretch exponent, that accounts for the dynamic heterogeneity in the systems. Regardless of the model function chosen, one can always extract the width of the peak (i. e., HWHM). Dependence of HWHM on the momentum transfer vector is used to characterize the geometry of diffusion motion. In many cases, the HWHM, $\Gamma_i(Q)$, is related to momentum transfer (Q) as:

$$\Gamma_i(Q) = \frac{D_i Q^2}{1 + D_i Q^2 \tau_{o,i}} \quad (7)$$

where τ_o is the residence time between successive diffusion jumps and D is the diffusion coefficient. If there is no residence time ($\tau_o = 0$), the diffusion process is of Fickian type (continuous, as opposed to jump, diffusion). A finite value of residence time implies a jump diffusion process. In this case, the fitted diffusion coefficient can be used to evaluate the jump length associated with the jump diffusion process, L , as $L^2 = 6D\tau_o$. In practice, at first it is determined, oftentimes empirically through the data fitting, whether the QENS spectra at the measured Q values could be reasonably well described by a Lorentzian or a combination of Lorentzians as a function of E, or a more complicated, "stretched" functional form of the model scattering function as a function of E is necessary. Then it is determined whether the Q dependence of the fitted broadening parameter of the model scattering function (for a Lorentzian, simply its HWHM) can be described as a Fickian diffusion process, a jump diffusion process, or a more complicated diffusion process.

It should be noted that QENS signal is typically dominated by and essentially probes the hydrogen-bearing cations of RTILs, whereas the anions that lack hydrogen atoms make a relatively small contribution to the scattering signal.

Quasielastic neutron scattering studies of room-temperature ionic liquids in supercapacitor electrode materials

Ionic liquids are non-volatile, thermally stable, and electrically conductive liquids of low melting points comprised of dissociated cations and anions. The structure of many room temperature ionic liquids has been investigated by x-ray and neutron scattering techniques.^{66, 67} These studies have revealed a self-assembled nanostructure in a wide range of ionic liquids. Solvophobic segregation of ionic liquids results in a formation of nanometer-scale structures due to the presence of polar anions and the cations with polar head and long alkyl chain.⁶⁸ Nano structures in ionic liquids have also been observed using MD simulations.⁶⁹⁻⁷² These self-originated structural heterogeneities in bulk ionic liquids create complex dynamic environments to the ions. Therefore, dynamics of ions in ionic liquids can be expected to exhibit different types of relaxation processes, spawning different time and length scales. Microscopic dynamics of many ionic liquids in bulk form have been investigated using various techniques, such as dielectric spectroscopy, optical Kerr effect spectroscopy, electron spin resonance, pulsed-field-gradient spin-echo nuclear magnetic relaxation, and QENS.^{73, 74} Aside from QENS, other techniques mentioned above measure mostly the rotational, and in some cases both rotational and translational dynamics, but typically cannot reveal the geometry of the dynamics processes involved. Pulsed-field gradient NMR measures the self-diffusion coefficients associated with long-range ion mobility, but in most cases, the time scale it probes is not sufficient to capture the internal motion of ions. On the

other hand, QENS, which explores dynamics on nano- to picosecond time scales, can resolve both reorientation motions and long-range translational mobility of ions, and reveal mechanism of the dynamic processes involved, which we review in the following section.

Ionic liquids in bulk

RTILs are known to exhibit nano-phase separation in their bulk state and have a long-range ion pair distribution with layers of oppositely charged ions (all ions of the RTIL) forming ordered structure.^{67, 75} The complexity of the structure depends on the nature of the cations and anions. The ions are involved in different types of interactions impacting their mobility. Strong ionic attraction significantly reduces the motion of ions, resulting in an increase of the viscosity, which decreases the conductivity when RTILs are used as electrolytes. Therefore, it is imperative to understand the dynamics of ionic liquids at a molecular level for their applications in different fields, especially, in energy storage devices. Triolo *et al.*⁷⁶ employed QENS to investigate the dynamics of ionic liquids for the first time. They observed two different relaxation processes (fast and slow) in 1-n-butyl-3-methylimidazolium hexafluorophosphate ionic liquid. The fast process, which occurs on sub-picosecond time scale and is independent of momentum transfer (Q) and temperature, was attributed to the localized librational motion of the H atoms. The slow process was assigned to the conformational transitions of the cation that spans nanosecond time scale. Similar observations were made by Ribeiro *et al.*⁷⁷ on the same ionic liquid, BmimPF₆, as a function of temperature using quasielastic Raman scattering. Yamamuro *et al.*⁷⁸ used QENS to observe both the fast and slow processes in a series of ionic liquids with different anions and dipole moments. The same group reported the presence of a fast β process above the glass transition temperature (T_g) and a slow process involving the cation exhibiting simple diffusion behavior in a model ionic liquid, BmimCl.⁷⁸

After a few successful QENS studies of dynamics in prototype ionic liquids, other research groups investigated more complex ionic liquids in bulk state using QENS. Mamontov *et al.*⁶³ investigated the dynamics of N,N,N',N'-tetramethylguanidinium bis(perfluoroethylsulfonyl)imide ([H₂NC(dma)₂][BETI]) and reported the presence of four distinct dynamic processes in this ionic liquid. Two of those were the localized processes, observed below the melting temperature of the ionic liquid and attributed to the methyl group rotation and the protons of the -NH₂ group. Two other processes (fast and slow) appeared above the melting temperature and were attributed, respectively, to the localized and long-range translational motion of cations center-of-mass. Similar observations regarding two types of the center-of-mass motions were made in silver complex-based ionic liquids, Ag(propylamine)₂⁺[Tf₂N⁻] and [Ag(1-pentene)⁺][Tf₂N⁻] (Tf₂N = trifluoromethanesulfonyl), with an additional dynamic component originating from -NH₂/CH₂.⁷⁹ Combined molecular dynamics simulations and QENS studies of 1-ethyl-3-methylimidazolium bromide (EmimBr) by Aoun *et al.*⁸⁰ also demonstrated the presence of two types of relaxation mechanisms (reorientational and translational) in EmimBr. This group claimed that the restricted localized translational type of mobility which was observed in ([H₂NC(dma)₂][BETI])⁶³ was not present in EmimBr and believed that the faster motion originated from the localized β -relaxation of the alkyl chain. A study of dynamics in an ionic liquid with a long alkyl chain, (1-octyl-3-methylimidazolium chloride (C8mimCl)) by Yamamuro *et al.*⁸¹ showed a faster relaxation of the alkyl chain and a slower

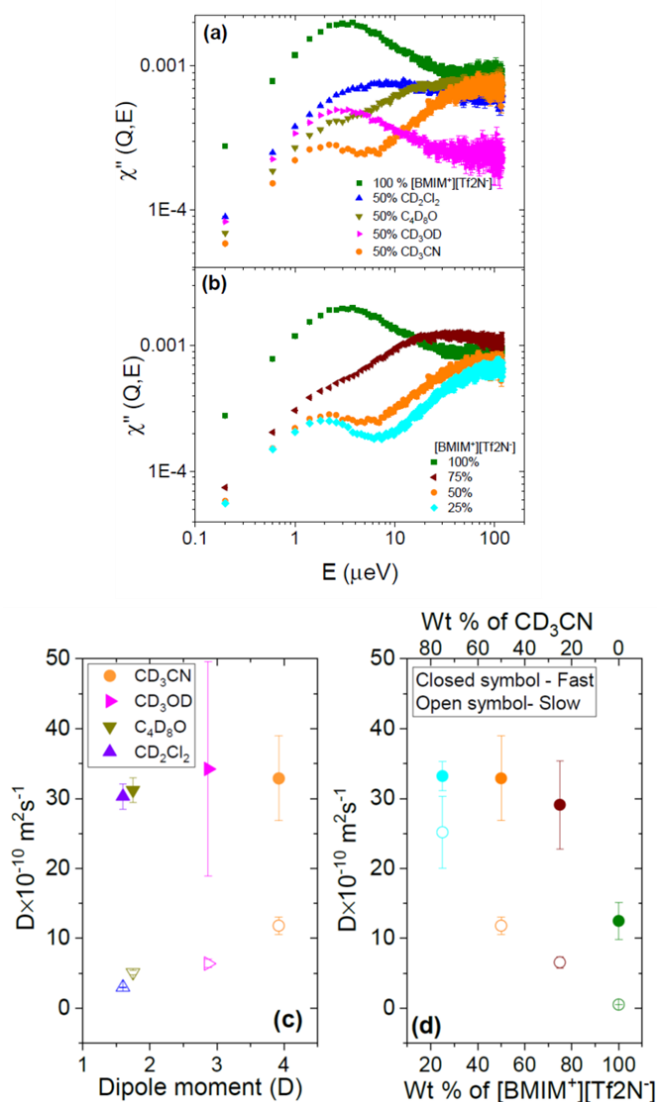


Fig. 2. Dynamic susceptibility of 1-butyl-3-methyl-imidazolium bis-(trifluoromethylsulfonyl), [BMIM⁺][Tf₂N⁻] generated by normalizing the QENS spectra to Bose occupation factor as described in the text, (a) as a function of dipole moments, and (b) with concentration of acetonitrile. Corresponding cation diffusivities are presented in (c) and (d). Reprinted with permission from J. Phys. Chem. Lett. 2017, 8, 167–171. Copyright 2017 American Chemical Society.

process involving the entire cation. Two dynamic processes, faster-localized and slower-diffusive, were also found in QENS studies of pyridinium based ionic liquids^{82–84} and protic ionic liquid⁸⁵. The same group observed enhancement of the localized dynamics of the alkyl side group on increasing the carbon chain length, whereas the opposite trend was reported for the translational motion of ions in N-alkylpyridinium-based ILs [C_nPy][Tf₂N] with n = 4, 5, 6, 7, 12.⁸⁶ In order to clarify the complexity of dynamics present in ionic liquids, Kofu *et al.*⁸⁷ investigated the dynamics of a series of imidazolium based ionic liquids, which have different anions and cations (of varied alkyl chain lengths), with QENS technique by employing two spectrometers, together covering the dynamics on 0.1 ps to 10 ns time scales. This extensive study revealed the presence of three relaxation processes in ionic liquids. The very fast process (on the time scale of ~ 1ps) was attributed to the reorientation of alkyl chain, which was found to be insensitive to the anions and the alkyl chain length. In contrast, out of the other two processes, one was from the relaxation of imidazolium ring, was

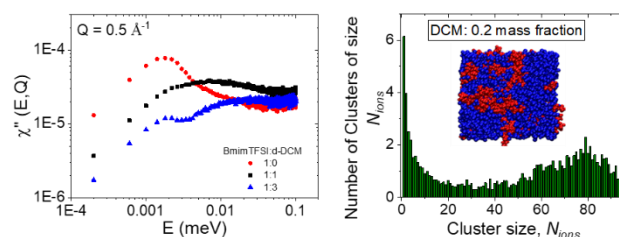


Fig. 3. (a) Dynamic susceptibility of 1-butyl-3-methyl-imidazolium bis-(trifluoromethylsulfonyl), [BMIM⁺][Tf₂N⁻] as a function of concentration of deuterated DCM. (b) Cluster analysis showing the dependence of number of clusters with cluster size, 1 to N_{ions} in 0.2 mass fraction of [BMIM⁺][Tf₂N⁻] in DCM. Inset is the corresponding MD snapshot. Reprinted with permission from J. Phys. Chem. C 2019, 123, 19354–19361. Copyright 2019 American Chemical Society.

restricted, and depended weakly on the anions, whereas the slowest process was found to be Q-dependent and resulted from the diffusion of ions. The activation energy of this long-range jump diffusive process was inversely related with the size of anions.

Mixing of ionic liquids with other ionic liquids, salts, co-solvents, or impurities provides a new platform to tune the properties of RTILs for different applications (specifically, energy storage) and is a focus of active research.^{88–92} The presence of two relaxation processes in an ionic liquid, (1-butyl-3-methyl-imidazolium bis-(trifluoromethylsulfonyl), [BMIM⁺][Tf₂N⁻]) was demonstrated (Fig. 2) by Osti *et al.*⁹³ by displaying the imaginary part of dynamic susceptibility, $\chi''(Q, E)$, obtained from the QENS spectra. Dynamics susceptibility is a response function that describes a small linear change on a system as a result of an external perturbation that depends on time and space. To display its imaginary part, the QENS spectra are normalized to the Bose thermal population factor, $n_B(E) = 1/(\exp(\frac{E}{kT}) - 1)$, as $\chi''(Q, E) = \frac{S(Q, E)}{n_B(E)}$. Bose thermal population factor is the number of scattering entities having a specific energy at a given temperature. This presentation displays various relaxation processes as separate peaks as a function of energy transfer and delivers a key information about the dynamics of materials at the molecular level. Regardless of the presence and concentration of co-solvents, they observed separation into an ionic liquid rich and a solvent rich phases in [BMIM⁺][Tf₂N⁻]/solvent mixtures, with the corresponding slow and fast cation dynamics evident from the two distinct peaks observed in the dynamic susceptibility spectra (Fig 2a and 2b). Furthermore, they also explored how the conductivity and ion dynamics of [BMIM⁺][Tf₂N⁻] change in mixtures with aprotic co-solvents of different dipole moments. Their studies showed an increase in conductivity of the ionic liquid as a function of increasing co-solvent concentration, reaching a maximum at 1:1 ratio of the liquid with the organic solvents. They obtained a linear relationship between the microscopic dynamics of the ionic liquid and the dipole moments and the concentration of organic solvents (Fig 2c and 2d). This relationship was correlated with the ability of solvents to screen the ion-ion interactions within the liquid, which scales with the energy associated with an ion pair separation, as evidenced by the MD simulations. In this study, they also showed an increase in the diffusivity of both the localized restricted and the long-range translational diffusion of ions as a function of increasing concentration and the dipole moments of organic co-solvents. Thompson *et al.*⁹⁴ subsequently employed a comprehensive computational screening approach to investigate the influence of other co-solvents properties, besides dipole moment, on the

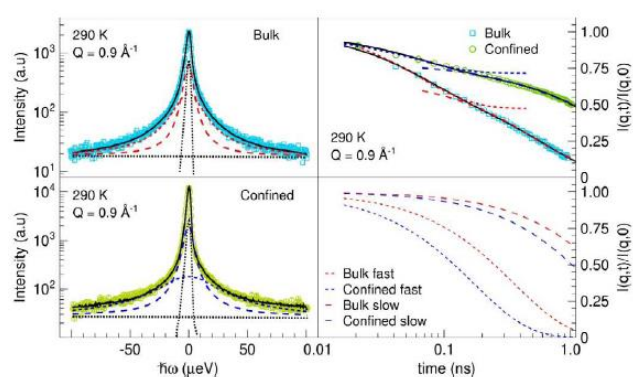


Fig. 4. Left panels: QENS spectra of [bmim⁺][Tf₂N⁻] in bulk (top) and confined (bottom) states together with the model fits at 290 K at a representative Q value (solid lines: two Lorentzian fits; dashed line: slow component; dotted lines: fast component; small dotted lines: instrument resolution; small-dotted straight line: background). Right panels: Normalized (at $t = 0$) Fourier transformed QENS spectra of bulk and confined ionic liquid along with the fits showing fast decay (bottom panel) of the spectra as a function of time for the confined ionic liquid. Reprinted with permission from EPL, 97 (2012) 66004. Copyright 2012 EPL IOP Publishing.

diffusivity of 1-butyl-3-methylimidazolium bis-(trifluoromethanesulfonyl)imide ([BMIM⁺][Tf₂N⁻]) ions in its mixtures with 22 different solvents. They concluded that the mobilities of ([BMIM⁺] and [Tf₂N⁻]) ions depend heavily on the pure solvent diffusivity. Osti *et al.*⁹⁵ tested these MD simulations results experimentally by selecting four organic solvents of similar polarities, but different bulk diffusivities. From QENS measurements using two neutron scattering spectrometers and MD simulations, they found a nanophase separation into ionic-rich and solvent-rich phases, as evidenced by a single peak in the susceptibility plot of pure ionic liquid that splits into two peaks when the solvent concentration is

increased to 20% or higher (Fig. 3a). This phase separation is illustrated by an MD simulation snapshot (Fig. 3b, inset) together with the cluster analysis presented in Figure 3b. Furthermore, they also found a strong influence of diffusivity of pure organic solvent on the long-range translational mobility of the cation, which becomes more pronounced for the ions in the solvent-rich phase.

To summarize the results of QENS studies of bulk RTILs, the intra-particle dynamics, which is highly ion-specific (e.g., related to the cation alkyl chain), manifests itself on the faster side of QENS sensitivity range (sub-picoseconds to picoseconds). On the other side of sensitivity range, spanning characteristic times from tens of picoseconds to nanoseconds, there are center-of-mass motions that generally exhibit a faster component due to localized motions and a slower component linked to long-range translational diffusivity. The slower components generally exhibit stronger temperature dependence.⁶³ The unique sensitivity to all center-of-mass motions, both localized and translational, which are closely linked to the transport properties, is a general feature of QENS measurements of liquids,^{63, 96, 97} not specific exclusively to RTILs. For RTILs in their bulk states, molecular dynamics simulations^{98, 99} of imidazolium, pyrrolidinium, and pyridinium based ionic liquids have supported existence of both localized and long-range translational diffusion of ions. However, the microscopic dynamics of ionic liquids becomes significantly different in confinement, which we will review in the following section.

Ionic liquids in in carbon-based electrode materials for supercapacitor

s

Table 1 A list of ionic liquids and the porous carbon systems studied by QENS

[bmim ⁺][Tf ₂ N ⁻]	Ordered mesoporous carbon	103
[H ₂ NC(dma) ₂][BETI]	Ordered mesoporous carbon	106
[EMIM][Tf ₂ N], [HMIM][Tf ₂ N], [EMIH][Tf ₂ N], and EmimBF ₄	Onion-like carbon	107, 130
[EMIM][Tf ₂ N]	TiC derived carbon; defunctionalized, hydrogenated and aminated.	111
[EMIM][Tf ₂ N]	SiC derived carbon; defunctionalized and Oxygen rich Non-porous system: graphene nanoplatelets	112
[emim][Tf ₂ N]	Under applied electric field Meso and micro porous carbon matrix	133
[BMIm ⁺][Tf ₂ N ⁻] and [OMIm ⁺][TFSI ⁻]	Mo ₂ C derived carbons	115, 123
[EMIM ⁺][Tf ₂ N ⁻], [BMIM ⁺][Tf ₂ N ⁻], and [HMIM ⁺][Tf ₂ N ⁻]	SiC derived carbon	119
C3mimTFSI and C12mimTFSI,	Ordered mesoporous carbon	120
[EMIm ⁺][Tf ₂ N ⁻]	MXene (Ti ₃ C ₂)	161

Cations: N,N,N',N'-tetramethylguanidinium = [H₂NC(dma)₂]; EMIM or EMIm⁺ or Emim⁺ = 1-ethyl-3-methylimidazolium; EMIH = 1,6-bis(3-methylimidazolium-1-yl) [bmim⁺] or Bmim or BMIM⁺ = 1-butyl-3-methylimidazolium; HMIM or Hmim⁺ = 1-hexyl-3-methylimidazolium; Omim⁺ or C8mim or C8mim⁺ = 1-octyl-3-methylimidazolium; C12mim = 1-dodecyl-3-methylimidazolium; **anions:** [BETI] = bis(perfluoroethylsulfonyl) imide; [Tf₂N⁻] or TFSI⁻ = bis(trifluoromethylsulfonyl)imide; BF₄⁻ = tetrafluoroborate

Ionic liquids are confined in porous matrices for energy storage applications. Once they are confined inside the pores, their intrinsic properties, such as melting and boiling points, vapor pressure, and density depart significantly from the bulk values.

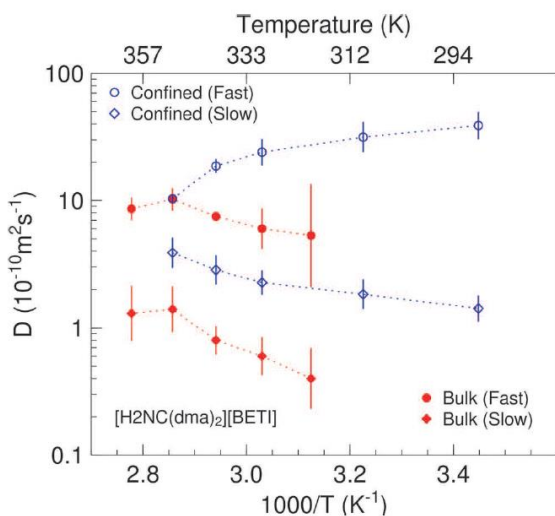


Fig. 5. Temperature dependent diffusivity of $[H_2NC(dma)_2][BETI]$ cations in bulk and confined states extracted from the QENS spectra collected from BASIS. Open symbols: confined $[H_2NC(dma)_2][BETI]$; filled symbols: bulk $[H_2NC(dma)_2][BETI]$; Circles represents the fast diffusivity and squares represents the slow diffusivity. Reprinted with permission from EPL, 102 (2013) 16004. Copyright 2013 EPL IOP Publishing.

Interactions between the ionic liquids and the surface of the charge/discharge processes in supercapacitors. The structure and dynamics of the electrolytes at SEI show the effects due to the pores shape and size and from the types of chemical species present on the surface of the electrode pores. Furthermore, the size of the ions (cation and anions), along with the chemistry of the ionic liquids, are the other factors that affect the performance of supercapacitors. In supercapacitors, ions adsorbed on the surface of the pores are responsible for the capacitance, whereas the mobility of the ions inside the pores determines the rate handling capability.^{14, 100-102} The structure of the electro-absorbed ions, as well as their mobility away from the walls of the pores, presents a complex picture in EDLCs. In addition to this, charging and discharging significantly alters the arrangement of ions inside the pores. QENS has been successfully employed to different experimental conditions. A list of the investigated ionic liquids and carbon matrices is presented in Table 1.

The first QENS experiment on an ionic liquid, $[bmim^+][Tf_2N^-]$, confined in a mesoporous carbon (pore sizes = 8.8 ± 2.1 nm in diameter) was performed by Chathoth *et al.*¹⁰³ using the backscattering silicon spectrometer (BASIS).¹⁰⁴ This neutron spectrometer, which has an energy resolution of 3.5 μ eV at the elastic line and resolves the dynamics on a few

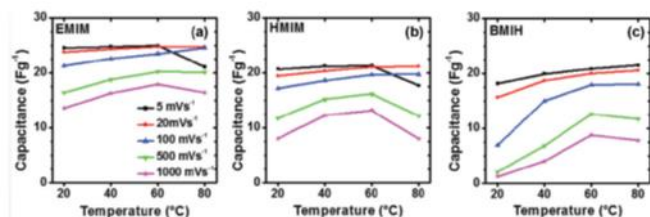


Fig. 6. Capacitance of three different ionic liquids with cations (a) [EMIM], (b) [HMIM], and (c) [BMIH] and a common $[Tf_2N^-]$ anion as a function of temperature at scan rates from 5 – 1000 mVs^{-1} scan rates. Reprinted with permission from J. Phys.: Condens. Matter 26 (2014) 284104. Copyright 2014 IOP Publishing Ltd.

picoseconds to a fraction of nanosecond time scale with a momentum transfer coverage of 0.2 \AA^{-1} to 2.0 \AA^{-1} , has been used in numerous QENS studies of bulk and confined RTILs. Similar to the bulk ionic liquid systems studies,^{63, 79} the study by Chathoth *et al.* showed the presence of two dynamic processes (slow and fast) in the ionic liquid confined in the mesopores. The slower process was attributed to the long-range translational diffusion of the cations, whereas the faster process was assigned to the spatially localized mobility of the cations. More interestingly, this work revealed a more pronounced broadening of the quasi-elastic spectra measured from the confined ionic liquid compared to the spectra of the bulk liquid (Fig 4, left side). This increased mobility of the confined ions resulted in shorter relaxation times compared to the ions in bulk state. This conclusion became more evident from the display of the decay of the $I(Q,t)/I(Q,0)$ as a function of the Fourier time derived from the QENS data, as presented in the bottom right panel of Fig 4. A detailed analysis of the QENS spectra showed an increase in diffusivity for a fraction of cations in the confined ionic liquid compared to the bulk counterpart at all the measured temperatures. This higher diffusivity for a fraction of cations was attributed to the excess (compared to the bulk state) density of cations near the pore walls, which leaves fewer cations in the middle of the pores, allowing for their faster diffusion. The faster diffusion of ionic liquids in mesoporous carbon has also been well demonstrated by Pinilla *et al.*¹⁰⁵ using MD simulations. Furthermore, Chathoth *et al.*¹⁰⁶ also reported the existence of two diffusion processes in an ionic liquid, $[H_2NC(dma)_2][BETI]$, confined in the similar type of mesoporous carbon. Since the pore size was similar to the one investigated in ref. (103), whereas the cations and anions were different, their study suggested that an increase in long-range diffusivity for a fraction of cations of an ionic liquid in nano-confinement may be a general feature of RTILs. Besides, they also reported an unusual situation where the localized restricted fast motion of $[H_2NC(dma)_2][BETI]$ confined in mesoporous carbon slowed down as a function of increasing temperature (Fig. 5). This unusual temperature dependence was rationalized based on the structural modification of the adsorbed ions, when the layered structure of the RTIL near the pore walls dissipates at higher temperatures to give rise to the bulk-like RTIL structure.

Van Aken *et al.*¹⁰⁷ investigated, for the first time, the dynamics of ionic liquids confined on the surface of carbon particles and established a correlation between cation mobility and electrochemical performance. They used onion-like carbon (OLC) particles of 5-7 nm in diameter with interparticle space of 3-20 nm, synthesized by high temperature annealing of nanodiamond precursor.¹⁰⁸ They employed QENS, together with electrochemical impedance spectroscopy (EIS) and MD simulations, to explore the impact of cation type on the dynamics and electrochemical performance of ionic liquids

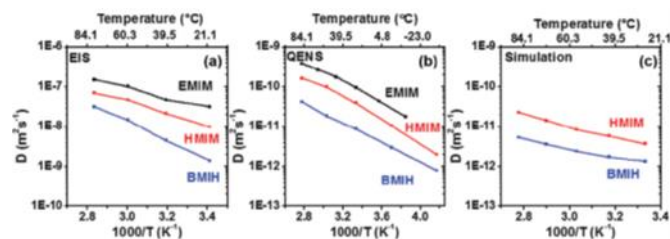


Fig. 7. Cation size dependent diffusivities of ionic liquids as probed by QENS (b). Similar trends were obtained from EIS (a) and MD simulations (c). Reprinted with permission from J. Phys.: Condens. Matter 26 (2014) 284104. Copyright 2014 IOP Publishing Ltd.

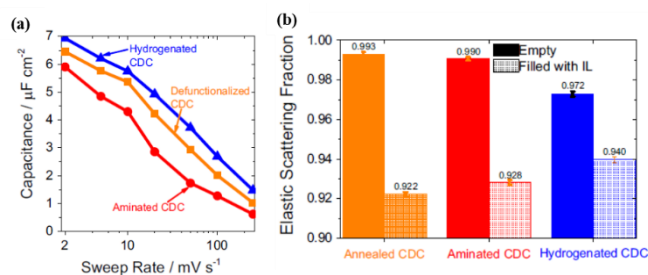


Fig. 8. (a) A comparison of rate handling ability of three CDCs with different surface functional groups with neat $[\text{EMIm}^+][\text{TFSI}^-]$ as electrolytes. (b) Corresponding elastic scattering fraction of those CDCs obtained from QENS data before and after loading with $[\text{EMIm}^+][\text{TFSI}^-]$. Reprinted with permission from *J. Phys. Chem. C* 2016, 120, 8730–8741. Copyright 2016 ACS Publishing.

featuring the same anion. For this study, three ionic liquids were chosen, with $[\text{EMIM}]$, $[\text{HMIM}]$, and $[\text{BMIH}]$ as cations and $[\text{Tf2N}]$ as the anion. The size of the cations was in the increasing order of $[\text{EMIM}] < [\text{HMIM}] < [\text{BMIH}]$. They showed an increasing trend in capacitance (Fig. 6) by the three ionic liquids in the order of their decreasing cation size at all measured temperatures and scan rates. The increase in capacitance of supercapacitors, involving ionic liquids and OLCs, as the temperature is increased,¹⁰⁹ has also been demonstrated from MD simulations. Furthermore, this increasing trend of capacitance with the decreasing cation size is correlated with the increasing diffusivities (Fig 7) as the cations become smaller, which is demonstrated by QENS, EIS, and MD simulations. Faster diffusivities obtained from EIS measurements, compared to QENS and MD simulations, were associated with the applications of the electric field during the measurements. Small discrepancies between MD and QENS values were attributed to the neutral systems, together with a simplified model, considered in the MD simulations.

A structural study of $[\text{C4mim}^+][\text{Tf2N}^-]$ confined in carbon substrate of an hierarchical porous structure by Bañuelos *et al.*¹¹⁰ showed the strong impact of the pore size to ion size ratio and the attraction between the ions and the surface of the wall on the density of the ionic liquid confined inside the pores. In addition to the ion-pore size ratio, the presence of chemical species on the pore wall or on the particle surfaces controls the surface-ions interactions, impacting the charge storage mechanism of supercapacitors. In order to understand the influence of surface chemistries on the dynamics of ionic liquid and on electrochemical performance, Dyatkin *et al.*¹¹¹ looked at the mobility of $[\text{EMIm}^+][\text{TFSI}^-]$ confined on the surface of the TiC derived carbons (CDCs). They have used three different CDCs with roughly the same pore size distribution, but different surface chemistries. The use of CDCs with identical porosities but of different surface chemistries allowed them to decouple the pore size effect from the molecular interactions that exist between the ionic liquid and the CDCs surfaces. For that, they synthesized defunctionalized (annealed) CDCs by annealing the precursor at 1200°C. Two more CDCs, one hydrogen-rich (hydrogenated-CDC) and another nitrogen-rich (aminated-CDC) were also synthesized. All these three types of CDC pores were filled with $[\text{EMIm}^+][\text{TFSI}^-]$ using an identical approach. Electrochemical measurements showed a higher capacitance with a greater rate handling ability (Fig. 8a) of hydrogenated CDC compared to its defunctionalized and aminated forms. This higher capacitance of hydrogenated CDC was attributed to the adsorption of greater numbers of $[\text{EMIm}^+][\text{TFSI}^-]$ cations on the pore surface, as revealed by the higher observed value of the

elastic scattering fraction (Fig. 8b) from QENS measurements. In a QENS measurement of a liquid, the scattering signal that appears elastic (that is, observed within the resolution function) is due to either the matrix, or the immobilized (on the time scale defined by the spectrometer energy resolution) particles, usually in direct contact with the matrix. Bulk-like liquids give rise to no elastic signal in QENS measurements. Thus, the fraction of elastic signal is proportional to the fraction of immobilized cations. The variation in the fraction of cations immobilized on the CDC surface demonstrates that the interactions between the cation and the surface of hydrogenated CDC is the most favorable among the three samples. Therefore, cations are retained strongly, resulting in a higher elastic scattering fraction, which in turn, provides a higher capacitance. Since more ions are attracted to the wall of the hydrogenated CDC, there are also relatively more ions which can move freely, providing an improved rate handling capability. This study highlighted the impact of surface chemistries on the electrochemical performance of ionic liquids in confinement.

In order to expand understanding of the surface chemistry impact on ions adsorption and electrochemical performances of ionic liquids-carbon based supercapacitors, Dyatkin *et al.*¹¹² investigated the influence of surface oxidation on the electrochemical performance and ion dynamics of $[\text{EMIm}^+][\text{TFSI}^-]$ confined in oxidized and defunctionalized silicon carbide derived porous CDCs using inelastic and quasielastic neutron scattering techniques together with MD simulations and electrochemical measurements. Similar to hydrogenated-CDC systems,¹¹¹ they observed a higher capacitance (Fig 8a) and the rate handling ability for ions confined in oxidized CDC due to accumulation of a larger number of ions on the surface of the oxidized pores. Oxidized surfaces are ionophilic and attract anions strongly, making a compact layer of cations next to them. This is further confirmed by the higher elastic scattering fraction from the QENS measurements observed for the ions confined in the oxidized pores compared to those in defunctionalized pores. The cations, which are firmly bound to the surface-bound anions, remain immobile and contribute to the elastic scattering on the time scale of the measurements. Densification of such cations on the surface of the electrodes has been observed in the atomistic MD simulations of nano-confined imidazolium-based ionic liquid.¹¹³ When most of the cations are held stationary on the pore walls, a few cations remain in the center of the pore. They are free to move within the free space available away from the pores wall. This conclusion is supported by the higher values of extracted HWHM (half width at half maximum) of the QENS signal collected from $[\text{EMIm}^+][\text{TFSI}^-]$ filled oxidized pores compared to defunctionalized pores, confirming the higher mobility of ions, which is responsible for the higher rate handling capability in the oxidized pores. QENS results further highlighted the fact of obtaining improved capacitance from the ionic liquid particles arrested in the oxidized CDC, due to the accumulation of more immobile cations on the surface of the pore walls, as illustrated by the higher values of elastic scattering fraction (Fig 8b) from the ions filled in the ionophilic (hydrogenated-CDC) pores.

Most of the ionic liquid-CDC systems that we have discussed so far used ionic liquids with ions roughly matching the pore sizes of the carbon substrate. Those CDCs have a unimodal pore size distribution, where pore sizes are on the order of ~ 1 nm. Control over the pore sizes and their distribution together with

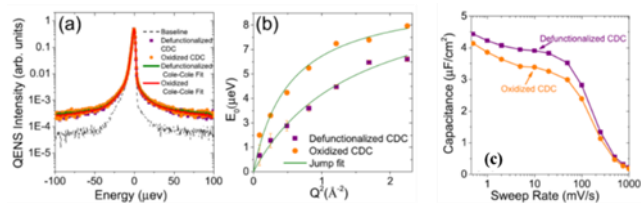


Fig. 9. (a) A comparison of QENS spectra of [OMIm⁺][TFSI⁻] confined in oxidized and defunctionalized Mo₂C-CDC pores along with a Cole-Cole model fit represented by solid lines, (b) Dependence of QENS width as a function of Q² obtained from the model fit. Solid lines represent a jump diffusion model fit. (c) SAA normalized capacitance confined in oxidized and defunctionalized pores. Reprinted with permission from Carbon 129 (2018) 104e118. Copyright 2017 Elsevier Ltd.

the pore surface chemistries depends on the Cl₂ etching conditions applied to the precursor metal carbides. By altering the synthesis procedure, one can control the CDCs pore size and surface chemistries that ultimately allows to manipulate the ion density inside the pores.¹¹⁴ Several studies^{107, 111, 112} have explored the ion dynamics in ionic liquids confined either in uniform micropores or uniform mesopores of carbon substrate (with a monomodal pore size distribution). Those studies have used ionic liquids with the dimensions of the ions roughly matching the nano pore sizes. However, there are many ionic liquids with asymmetric ions (i.e., when the cation is significantly larger than the commonly used anion). Control over etching conditions facilitates production of CDCs with bimodal pore distribution (having micropore and mesopores within the same CDC substrate). Electrochemical performance together with the ion dynamics of an ionic liquid having significantly longer alkyl chain, 1-octyl-3-methylimidazolium bis(trifluoromethylsulfonyl)imide ([OMIm⁺][TFSI⁻]) confined in molybdenum carbide (Mo₂C) derived CDC with varied surface chemistries (oxidized and defunctionalized) and bimodal pore size distribution has been investigated by Dyatkin *et al.*¹¹⁵ The choice of Mo₂C allowed production of CDCs with both micropores and mesopores because of the large size of the molybdenum atom (compared to Ti and Si atoms), where the dimension of the micropores is suitable for holding anions, and the mesopores are suitable for holding cations with bulky alkyl chain, [OMIm⁺]. QENS spectra (Fig. 9a) reflecting the contribution of OMIm⁺ cations reveal a faster mobility (higher values of HWHM, Fig 9b) of the ions confined in the oxidized pores from the data analysis using Cole-Cole distribution model scattering function. Similar to the dynamics of [EMIm⁺] confined in functionalized SiC-CDC pores,¹¹¹ this study attributed the faster diffusivity of cations to the less densely packed ions in the center of the pores originating from a complete wetting of the

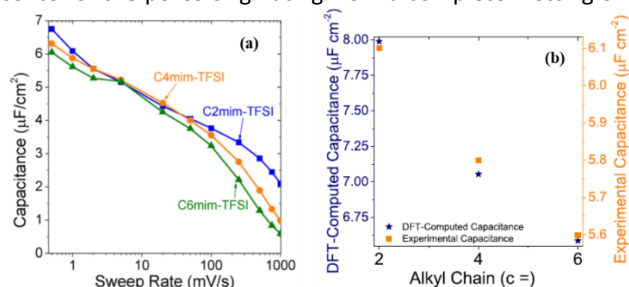


Fig. 10. (a) Electrochemical performances of C_nmimTFSI (n = 2, 4 and 6) confined in SiC-CDC of nano pores. (b) A comparison of CDFT calculated capacitance with the experimentally measured capacitance obtained from cyclic voltammetry. Reprinted with permission from Electrochimica Acta 283 (2018) 882e893. Copyright 2018 Elsevier Ltd.

oxidized pores by [TFSI⁻] anions, which draw more [OMIm⁺] cations towards the pore walls. A larger number of cations immobilized on the pore surfaces of the oxidized pores contributed 6-14% more to the elastic scattering fraction compared to the same amount of [OMIm⁺][TFSI⁻] confined in defunctionalized Mo₂C-CDC pores. [OMIm⁺] in defunctionalized pores shows a reduced mobility because of the higher density of the ions in the center of the pores. However, unlike for the ionic liquid in functionalized CDC pores of uniform porosity,¹¹¹ the SSA normalized capacitance (Fig. 9c) measured from [OMIm⁺][TFSI⁻] confined in oxidized Mo₂C-CDC of bimodal pore size distribution is smaller than the capacitance from the defunctionalized pores. This observation agreed with the MD simulation results, but contradicted the previous findings.¹¹¹ The result was understood as originating from the minimum charge densities of cation away from the pore walls resulting from a strong attraction of anions (TFSI⁻) towards the surfaces. At the same time, there is a repulsion of hydrophobic [OMIm⁺] ions, causing a significant reduction in the number density of electro-adsorbed ions on the surfaces.

Apart from modifications of the surface chemistry and topological characteristics of electrode materials to optimize electrochemical performances in device applications, molecular parameters of ionic liquids are the other controlling factors that can be altered to improve electrochemical devices' performance. For example, viscosity and melting points of ionic liquids can be tuned simply by changing the molecular dimensions of the ions.¹¹⁶⁻¹¹⁸ When changing the alkyl chain length of the cation of the imidazolium based ionic liquids, their viscosity, together with the conductivity, can be modified. These modifications allow to selectively tune the size of the ions based on the pore size of the electrodes to optimize the rate handling ability and capacitance of EDLCs. Dyatkin *et al.*¹¹⁹ investigated the influence of the length of alkyl chain attached to the cation of an imidazolium based ionic liquid on the ion dynamics along with the electrochemical performance in SiC-CDC based supercapacitors by employing QENS, electrochemical measurements, and MD simulations. For this investigation, they used three imidazolium-based ionic liquids that have the same anion, TFSI⁻, but different cations with ethyl (n = 2), butyl (n = 4), and hexyl (n = 6) groups attached to the imidazolium ring. This comprehensive approach of probing the dynamics of ions confined in CDC with narrow pores (0.8 nm) in the absence of applied potential has revealed a monotonic decrease in the long-range cation diffusivity on increasing the alkyl chain length as evidenced by QENS measurements. A diffusion coefficient of C2mim⁺ was found to be $2.83 \pm 0.34 \times 10^{-10} \text{ m}^2 \text{ s}^{-1}$, which decreased by a factor of three, to $0.92 \pm 0.05 \times 10^{-10} \text{ m}^2 \text{ s}^{-1}$, when the number of carbons on the chain was increased by four. However, there was only a very small decrease in the diffusivity when moving from C2mim to C4mim, which, for the latter cation, was $2.32 \pm 0.22 \times 10^{-10} \text{ m}^2 \text{ s}^{-1}$. The capacitance (Fig. 10a) and the electro-sorption dynamics (in the presence of potential) from electrochemical measurements also showed similar trends as a function of the alkyl chain length. Consequently, the alkyl chain length effects were more impactful at higher sweep rate, where the chain length influence was relatively similar between C4mimTFSI and C6mimTFSI compared to C2mimTFSI. On the other hand, they found a similar behavior between C2mimTFSI and C4mimTFSI compared to C6mimTFSI in their electro-sorption resistance

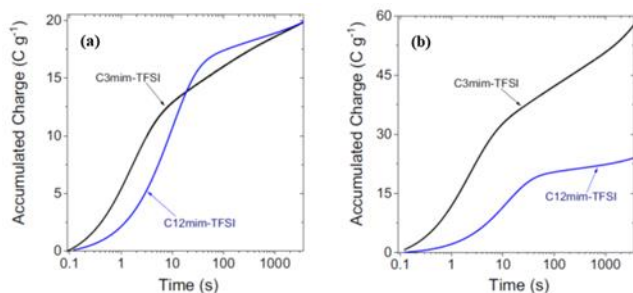


Fig. 11. A comparison of charging of C3mimTFSI and C12mimTFSI from square-wave chronoamperometry under applied voltages (a) up to 1.0 V. (b) to 2.0 V. Reproduced with permission from J. Electrochem. Soc., 166 (4) A507-A514 (2019). Copyright 2019 The Electrochemical Society.

near-static potential. MD simulations (Fig. 10b) have further confirmed the observations made with QENS and electrochemical measurements.

To further understand the influence of the alkyl chain length on the electrochemical performance and the electrodynamics of ionic liquids in supercapacitors, Osti *et al.*¹²⁰ examined the fundamentals of ion dynamics and electrosorption of two imidazolium-based ionic liquids of different cation length (C3mim⁺ and C12mim⁺) and of same anion (TFSI⁻), by confining them in ordered mesoporous carbon (OMC) having both micro and mesopores. They investigated the impact of alkyl chain length on the dynamics of cation and studied the influence of those dynamics on the capacitive behavior of the supercapacitors using QENS, electrochemical measurements, and cDFT calculations. They found that the size of cation had a major impact on the electrochemical behavior, especially the rate handling and impedance, while the applied potentials were found to control the wetting/filling (charge storage) of the pore walls, particularly, for the ionic liquid with the larger cation (Fig. 11a and 11b). Results from cDFT calculations using a coarse-grained model corroborated the electrochemical observations, showing a 16% decrease in capacitance on increasing the alkyl chain length from C3 to C12. They employed QENS to probe the mobilities of both the C3mim⁺ and C12mim⁺ cations confined in OMC. They expected to observe the dynamics on different time

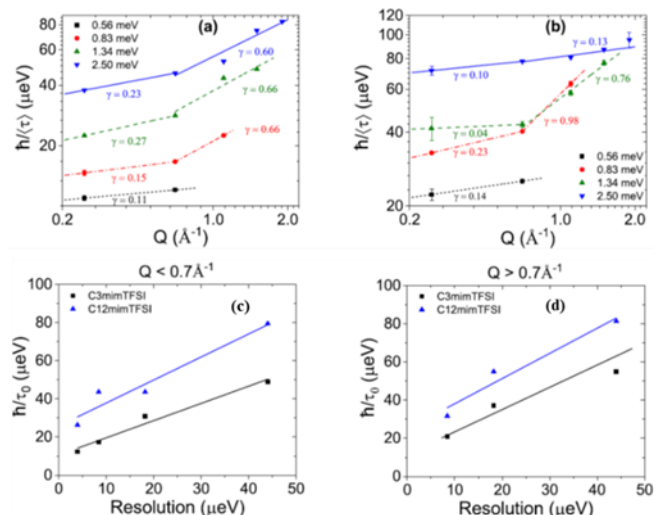


Fig. 12. A dependence of HWHM of QENS signal of (a) C3mimTFSI (b) C12mimTFSI with Q where γ is the slope of the lines fitted with the relation, $\langle\tau\rangle = \tau_0 Q^{-\gamma}$. (c) and (d) are dependence of corresponding structural relaxation time with instrument resolution. Reproduced with permission from J. Electrochem. Soc., 166 (4) A507-A514 (2019). Copyright 2019, The Electrochemical Society.

scales when the alkyl chain becomes longer; therefore, a cold neutron multi-chopper spectrometer (LET)¹²¹ was used to perform the dynamic measurements. Using the repetition rate multiplication capability of the spectrometer, they observed localized dynamics of cations confined in pores (based on the Q -independent broadening of the dynamic susceptibility peaks) for both C3mim⁺ and C12mim⁺ cations. Interestingly, using analysis of QENS data with the Cole-Cole distribution model scattering function, they observed a higher value of HWHM (Fig. 12a and 12b) from C12mim⁺, suggesting a higher mobility coming from the larger ions, which is surprising in the view of the established fact that the bigger ions generally move slower.

Furthermore, non-quadratic dependence of the extracted HWHM (Fig. 12a and 12b) on the Q , observed for both C3mim⁺TFSI⁻ and C12mim⁺TFSI⁻ confined liquids, ruled out a possibility that the long-range diffusivity might have been

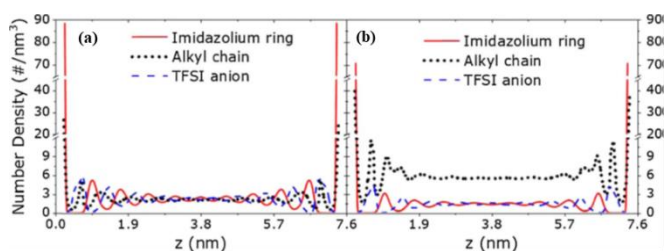


Fig. 13. A dependence of number density for (a) C3mimTFSI and (b) C12mimTFSI as a function of a distance away from the pore walls in mesopores of 7.6 nm diameter. Reproduced with permission from J. Electrochem. Soc., 166 (4) A507-A514 (2019). Copyright 2019, The Electrochemical Society.

observed in the experiment, suggesting instead the observation of a spatially confined motion of the ions. A weaker Q -dependence of the average relaxation time of the ions confined in mesopores (> 1 nm) suggests the dynamic decoupling of alkyl chain from the imidazolium ring, therefore giving rise to the higher mobility observed from the ions with longer alkyl chain. This concept of dynamics decoupling in cations with a longer alkyl chain has been further proved by calculating the structural relaxation time, τ_0 . The relaxation time was found longer for C3mim⁺ and was instrument resolution dependent (Fig 12c and 12d), confirming that the relatively faster motion in C12mim⁺ originated from the undulation of the chain, completely decoupled from the ring dynamics. This decoupling was proved by calculating the number density from cDFT that showed density spikes for C12mim⁺ (Fig. 13a and 13b) away from the walls, towards the center of the mesopores, where interactions are weak between the ions and the pore walls.

Most of the ionic liquids undergo nano-phase separation, due to the presence of different interactions that exists within the ionic liquids, giving them a higher viscosity, which severely impacts the conductivity of ionic liquids. The low conductivity associated with ionic liquids originates from the reduced ion mobility, which also significantly lowers the rate handling capability in supercapacitors. Not only in the bulk state, but also in confinement, an increase in conductivity of ionic liquids can be achieved by mixing them with salts, organic solvents, and other ionic liquids.^{91, 93} Mixing those components remarkably changes the physicochemical properties of the ionic liquids by disrupting the interionic Coulombic interactions. This is one way of formulating a new electrolyte with improved properties for energy storage applications. On the other hand, the use of

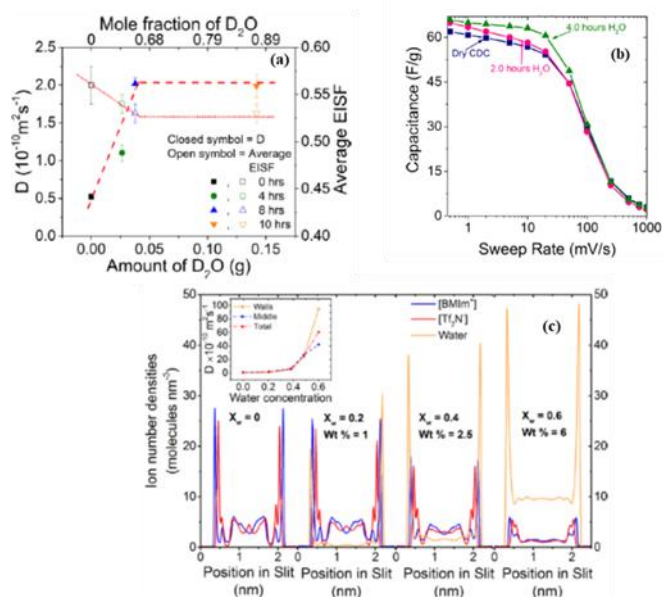


Fig. 14. (a) Cation diffusion coefficients of [BMim⁺][Tf₂N⁻] as a function of D_2O exposure time/uptake along with corresponding EISF. Solids lines are a guide to the eye. (b) Corresponding electrochemical performances in terms of rate handling ability. (c) Number densities profile of ions and water calculated from the confined ionic liquid at different mole fraction of water. Reprinted figures with permission from Phys. Rev. Mater 1, 035402 (2017). Copyright 2017 by the American Physical Society.

inorganic solvents, such as water, is found to accelerate the nano aggregation in ionic liquids.¹²² Osti *et al.*¹²³ attempted to investigate the electrochemical performance of an ionic liquid, [BMim⁺][Tf₂N⁻], confined in Mo₂C-CDC of pores (0.7-3.1 nm) under the influence of water (D_2O was used for neutron scattering measurements due to the smaller scattering cross-section of deuterium) vapor using QENS, together with electrochemical measurements and MD simulations. QENS data analysis showed a direct effect of water uptake with a twofold increase in the cation diffusivity (Fig. 14a) after 4 hours of water vapor exposure. Even though the amount of D_2O absorbed by [BMim⁺][Tf₂N⁻] with a hydrophobic butyl chain in confinement is relatively high compared to its bulk state, it produces only a small decrease in the elastic incoherent scattering fraction, suggesting that most of the D_2O is absorbed on the CDC's wall, thereby displacing some of the BMim⁺ cation from the pores wall. They attributed the higher diffusivity of the cation, before the pores become totally saturated with water, to the combined impacts of both cation displacement and the screening of attraction between the ionic liquid molecules by water. These QENS findings were corroborated by an increase in the capacitance along with the rate handling (Fig. 14b) and a decrease in the ion densities (Fig. 14c) on the pores walls upon increasing the water content, as observed in the MD simulations.

Despite having properties superior to many organic and aqueous electrolytes used in EDLCs, RTILs still do not function well over the entire theoretically accessible voltage window.¹²⁴ This is due to the different activities of cations and anions on the surfaces of the electrodes. Those different activities result in an asymmetric working potential of EDLCs that limits their operational voltage window.^{125, 126} The asymmetry in

working potential has been corrected through the modifications of electrode materials.^{125, 127, 128} In 2015, Van Aken *et al.*⁹⁰ introduced a new concept of correcting the asymmetries by mixing two ionic liquids, with the same cations, but anions of different sizes and chemistries. They tested mixtures of EmimTFSI and EmimBF₄ at various compositions as electrolytes, using onion-like carbon (OLC) as electrodes in supercapacitor configurations. Their studies showed a balanced charge storage on identical OLC electrodes using 4:1 mixture of EmimTFSI and EmimBF₄, resulting in a symmetric supercapacitor. They postulated that the optimal mixture acts as a new electrolyte, having properties that are totally different from those of its individual constituents. Similar electrodes and electrolytes systems have been studied using the cDFT.¹²⁹ cDFT has shown a maximum capacitance at this 4:1 composition because of an increase in the contact density of the cation, Emim⁺, on the electrode surface, which resulted from the reduction of the layered structure due to the presence of smaller anions (BF₄⁻) under the applied potential. Osti *et al.*¹³⁰ explored the structures and dynamics of those ionic liquids (EmimTFSI and EmimBF₄) mixtures at various compositions using QENS and cDFT under zero applied potential. Their analysis of QENS data showed no significant changes in the diffusivities and phase behavior of bulk EmimTFSI and EmimBF₄ mixtures compared to the individual values for bulk EmimTFSI and bulk EmimBF₄. However, QENS data for the mixtures adsorbed on the OLC surfaces exhibited significantly different behavior. The average elastic scattering fraction, which represents the contribution of the cation adsorbed on the electrode surface, as obtained from QENS data analysis (Fig. 15a), showed a maximum at the optimal composition of 4:1 (EmimTFSI:EmimBF₄ = 4:1), which precisely correlated with the excess adsorption of the cation calculated from cDFT. This is evident from the QENS data for the 4:1 mixture of EmimTFSI and EmimBF₄ confined in OLC that

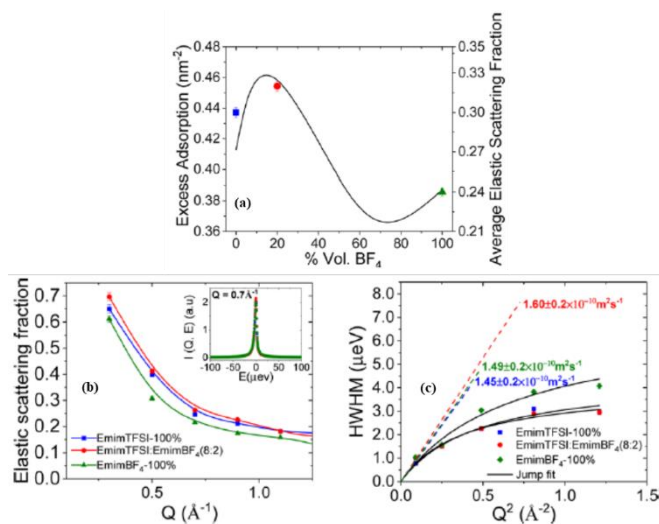


Fig. 15. (a) A comparison of excess cation, Emim⁺, adsorption on the OLC surfaces computed by cDFT under the absence of applied potential along with an average elastic scattering fraction obtained from QENS measurements (right y-axis). (b) Elastic scattering fraction as a function of Q along with a representative QENS spectra in inset. (c) Dependence of HWHM with Q^2 showing diffusivity values at different mixture compositions. Reprinted with permission from J. Phys. Chem. C 2018, 122, 10476–10481. Copyright 2018 American Chemical Society.

had a higher scattering intensity at the elastic line (Fig 15b inset). Data analyses also showed a higher elastic scattering fraction (Fig 15b) and a higher diffusivity (Fig 15c) of the Emim⁺ at 4:1 composition compared to the neat confined liquids. This was due to the adherences of a larger number of cations to the surface of the OLC, thus leaving more room for the remaining cations to move freely away from the electrolyte-electrodes interface, resulting in a higher diffusivity.

All the QENS experiments that we have reviewed so far were conducted on ionic liquids-filled carbon pores without applied potential. The structure of EDL, which largely controls the transport mechanism of nano confined fluids and thereby the performances of supercapacitors, changes significantly during charging and discharging of EDLC. Structural modifications of the EDL during charging have been studied by Lian *et al.*¹³¹ by employing the time-dependent density functional theory (TDDFT), taking electrostatic correlations and the ion's steric effects in account. They showed a non-monotonic increase of surface charge with an enhancement of dispersion interactions during charging. Furthermore, the discernment of ions and the partitioning in ionic liquids having various types of ions in a substrate of hierarchical pore structures become very influential in determining selectivity and packing, relative to the sizes of ions and their concentration, as demonstrated by cDFT.¹³² To understand the microscopic dynamics of nano-confined fluids under the influence of applied potential in a carbon substrate of hierarchical pore sizes, Mahurin *et al.*¹³³ investigated the dynamics of [emim][Tf2N] confined in porous carbons under an applied potential (charged and discharged states) using QENS and MD simulations. They performed an *in situ* QENS experiment by confining [emim][Tf2N] in two separate carbon electrodes, mesoporous (6.7 nm diameter pores) and microporous (1.5 nm diameter pores), in a custom-

built electrochemical cell. Diagnostic temperature-dependent scans showed bulk-like behaviors of [emim][Tf2N] confined in 6.7 nm pores, but severely suppressed mobility of [emim][Tf2N] in 1.5 nm pores. Furthermore, they observed a change in the elastic scattering intensity upon changing the applied potential without an appreciable modification on the quasielastic wings (insets in Fig. 16) of the spectra, thus verifying an impact of applied voltage on the dynamics of ions present near the pore walls. A similar cation immobilization on the electrode surfaces of silver and graphene has been observed under applied potential using the surface-enhanced Raman spectroscopy.¹³⁴ Elastic scattering intensities, as a function of applied potential from [emim][Tf2N] confined in 6.7 nm pores (Fig. 16a), showed a monotonic dependence on the applied voltage, resulting in a complete restoration of the originally measured elastic intensities after the removal of the applied potential. However, the experiments carried out at various temperatures and applied voltages (both negative and positive, Fig 16b-16d) showed that the initial immobilization of ions in microporous carbon (1.5 nm) is irreversible. Once the ions (either the cations or anions) are attached to those narrow pores by the initial application of potential, they remain static over hours and days long measurements, despite subsequent applications of a different potential. These observations are supported by the ions number densities calculated by the authors using MD simulations and further rationalized from the standpoint of the severely impeded in the 1.5 nm pores ion dynamics.¹³⁵

To summarize the results of QENS studies of RTILs confined in carbon-based electrode materials, most experiments show a separation of the scattering signal into the elastic and quasielastic part. The former originates from the ions adsorbed on the pore walls, with mobilities too low to be resolved on the nanosecond time scale, whereas the latter represents the mobile ions away from the pore walls. Manipulation of the electrode materials (via chemical functionalization or applied electric potential) can change the amount of the adsorbed ions, also indirectly influencing the packing of the remaining ions away from the pore walls and their diffusivity. Both the EDLC capacitance and rate handling can be influenced by these means.

Most of the EDLC systems that we have reviewed so far have ionic liquids confined either on the surface or inside the pores of carbon-based matrices, where the capacity is determined from the electrosorption of ions on the surface of the electrodes. Different approaches have been employed to boost the energy density of the capacitors. Besides employing hybrid devices, the use of layered materials that allow intercalation of ions between the layers has been explored extensively. These ions-intercalated layered electrodes exhibit high electrochemical performances in supercapacitors. The intercalation of ions depends on the chemical nature of the electrode surfaces, which ultimately determines the conductivity and hydrophobicity of the materials. The nature of chemical species present on the materials' surface determines the hydrophobicity, whereas the electron density of states is responsible for the conductivity. Most of the electrode materials used in supercapacitors are either hydrophilic, but

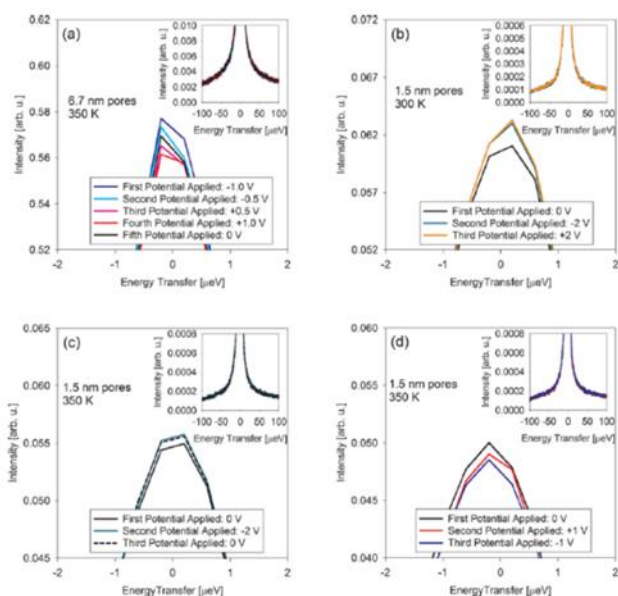


Fig. 16. Intensities of QENS signal near the elastic line from (a) [emim][Tf2N] confined in 6.7 nm carbon pores, (b-d) confined in 1.5 nm pores at various applied voltages and temperatures. Insets in each plot are QENS spectral wings. Republished with permission of American Institute of Physics, from Appl. Phys. Lett., 109, 143111 (2016). Copyright 2016 AIP Publishing Ltd.; permission conveyed through Copyright Clearance Center, Inc.

poor conductors, or hydrophobic, but highly conductive. In 2011, Naguib *et al.*¹³⁶ discovered 2D layered materials, called MXenes, which allow intercalation of different chemical species¹³⁷⁻¹³⁹ between the layers. MXenes are highly hydrophilic and conductive, which is a unique combination in 2D materials,^{136, 140} therefore, they have a broad potential range of applications, especially in energy storage.¹⁴¹ Within the short period of time following their invention, there has been a tremendous interest in MXenes that resulted in a synthesis of more than ~ 25 different MXenes. Many research papers and reviews of MXenes¹⁴¹⁻¹⁴⁶ focusing on synthesis, structure, and properties, based on experiments, DFT/ab initio computational effort, and theoretical approaches have been published. Here we intend to discuss the recent efforts to understand the structure and dynamics of ionic liquids confined in MXenes, in the context of ion dynamics and electrosorption of ions on the surfaces, investigated primarily by INS (inelastic neutron scattering) and QENS, which we review in the section below.

Ionic liquids in MXene electrode materials for supercapacitors

MXenes are early transition metal carbides, nitrides, or carbonitrides of two-dimensional layered structure, which are synthesized from a selective etching of aluminum (Al) from their MAX phases (where M = early transition metals, A = aluminum and X = C, N or C and N together).¹³⁶ The chemical nature of the etchants used to dissolve Al layer yields MXene with different surface terminations ($T_x = F, OH$ and O), allowing to intercalate a variety of chemical species between the MXene layers for a wide range of applications. A single molecular sheet of the MXene, which is made of carbides, nitrides, and carbo nitrides of transition metals, is called as a layer. When such layers are held together, they make a stack of MXene layers. The space between the two molecular sheets is an interlayers space (c-lattice), and that between the stacks is an inter-stack gap. Intercalation of metal ions and other chemical species in MXenes has been exercised extensively to achieve the desired material properties. Characterization and properties evaluation of those MXenes have been carried out using different techniques, which are well reviewed^{144, 147, 148} and not intended to be discussed here. Intercalation and confinement of fluids, primarily ionic liquids, in MXenes, and its effect on the structure and dynamics, together with electrochemical performance in supercapacitors, have recently attracted much interest,¹⁴⁸⁻¹⁵⁰ and we focus on these topics in the context of neutron scattering studies, specifically by INS and QENS. Both techniques are sensitive to the large incoherent scattering of hydrogen. INS probes the bonding between the surface termination groups of MXenes and the hydrogen-bearing chemical species, whereas QENS probes the motions (long range translational and localized) of the mobile species.

Intercalation of metal ions, as well as organic and inorganic species between MXene layers, has been a common practice to alter the materials' structure and properties for energy storage applications. Lukatskaya *et al.*¹³⁷ explored the impacts of cation intercalation on the capacitance of $Ti_3C_2T_x$ MXene for the very first time. They reported a high capacitance from MXenes

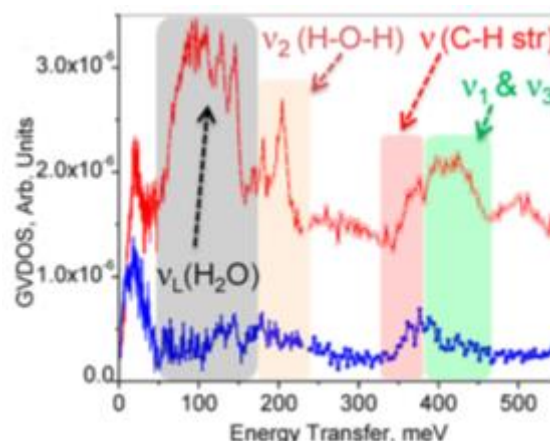


Fig. 17. Inelastic neutron scattering spectra collected from Nb₂C showing the generalized vibrational density of states from the sample after (blue) and before (red) annealing. Copyright © 2014, American Chemical Society.

intercalated with Na^+ , K^+ , NH_4^+ , Mg_2^+ , and Al_3^+ ions compared to the values obtained from the supercapacitors comprised of porous carbon electrodes. Mashtalir *et al.*¹³⁹ synthesized the organic molecules (hydrazine) intercalated MXene and studied its electrochemical performance in acid electrolytes. They reported a significantly increased capacitance from the hydrazine intercalated MXene compared to its pristine analog. Furthermore, the same group¹³⁸ investigated the intercalation, co-intercalation, and delamination behavior of different types of MXenes with hydrazine, N,N-dimethylformamide, and dimethyl sulphoxide. They reported an increase in the c-lattice parameter after intercalation of hydrazine, followed by a co-intercalation of N,N-dimethylformamide. They found a high capacity for Li-ions on the MXene paper (delaminated MXene sheets), produced after sonication of dimethyl sulphoxide intercalated MXene. An increase in the c-lattice parameter significantly reduces the van der Waals forces between the MXene layers, providing more surface area for ions (de)intercalation during charge-discharge processes. Relatively high in-plane conductivity, compared to out of plane, of MXene makes c-lattice parameter more important tunable parameters for the optimization of MXene properties. Xie *et al.*¹⁵¹ looked at the dependence of Li-ion storage capacity of MXene, based on the surface termination groups, and found the highest capacities in oxygen-terminated MXenes. They used inelastic neutron scattering for the first time on a MXene to figure out the state of water and the OH groups at a relatively high temperature. The absence of all the peaks (Fig. 17, blue curve) related to water and hydroxyl groups in the annealed samples indicates their removal at high temperature. Later on, Wang *et al.*¹⁵² used neutron total scattering in conjunction with multilevel structural modeling to reveal a complex structural pattern of MXene. INS has been employed to investigate the surface modifications of MXene after the intercalation of hydrazine between the layers by Mashtalir *et al.*¹³⁹ They found a significant amount of water with strong bonds with OH groups in the pristine MXenes. After intercalation of hydrazine, a large reduction of water and OH terminations, resulting in an increase in volumetric and gravimetric capacitance, has been reported. Furthermore, the decomposition of urea intercalated in $Ti_3C_2T_x$

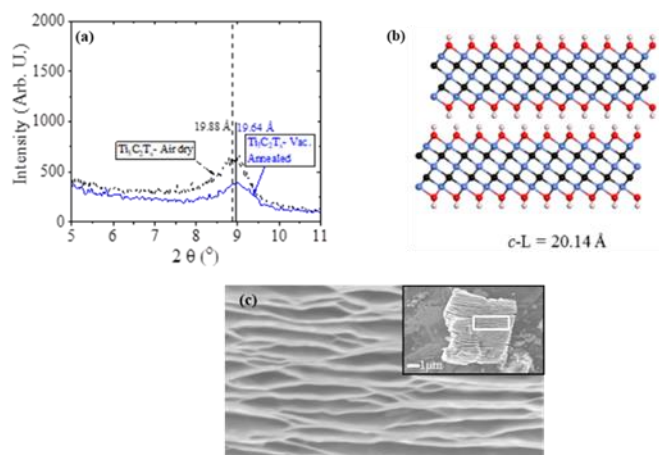


Fig. 18. (a) X-ray diffraction patterns of pristine $\text{Ti}_3\text{C}_2\text{T}_x$ MXene at two different states. (b) MD generated snapshot of bare MXene. (c) Zoomed SEM image of the mark region (inset) of pristine MXene. Reprinted with permission from ACS Appl. Mater. Interfaces 2016, 8, 8859–8863. Copyright 2016 American Chemical Society.

MXene to ammonium ions and carbon dioxide has been reported by Overbury *et al.*¹⁵³ using INS technique. Based on the INS results, they proposed formation of ammonium intercalated MXene from a rapid hydrolysis of urea during urea treatment of the MXene.

Water is one of the natural constituents originating from the synthesis that resides either in between the layers or in the inter-stacks gaps of MXenes. Structure and dynamics of water confined in MXenes have been explored using neutron scattering techniques. Osti *et al.*¹⁵⁴ started probing the dynamics of water confined between the $\text{Ti}_3\text{C}_2\text{T}_x$ MXene using a combination of QENS, x-ray, and MD simulations. The structure of the MXenes synthesized using 48% HF solution, in the air dried and vacuum annealed (110 °C) states, was investigated by x-ray diffraction (XRD). Diffraction patterns from both air dried and annealed samples (Fig. 18 a) have almost the same *c* lattice (*c*-L) parameters (19.88 Å and 19.64 Å, respectively). XRD derived *c*-L parameter matches well the *c*-L parameters obtained from ReaxFF molecular dynamics simulations (20.14 Å at 300 K) for a bare $\text{Ti}_3\text{C}_2\text{T}_x$ MXene (Fig 18 b). From this

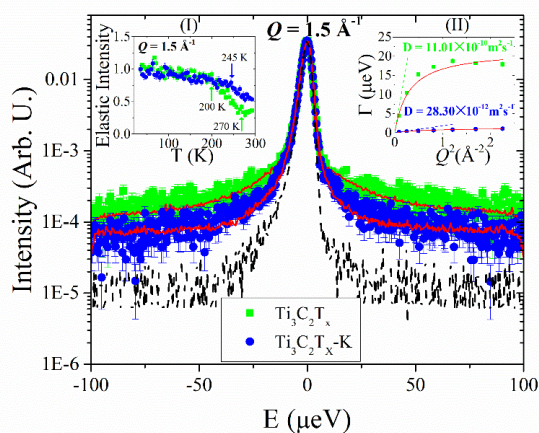


Fig. 19. QENS spectra at $Q = 1.5 \text{ \AA}^{-1}$ collected from pristine and K^+ ion intercalated MXenes. Insets I and II are corresponding elastic scan and widths of the spectra together with the diffusion coefficients of water evaluated using jump diffusion model, respectively. Copyright 2016 American Chemical Society.

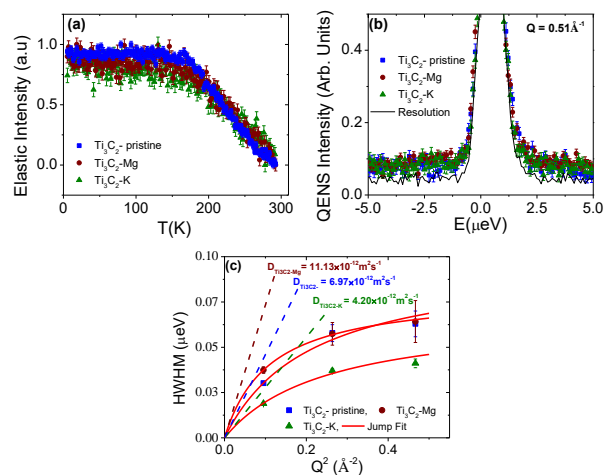


Fig. 20. (a) Normalized elastic intensities from dry pristine, Mg^{2+} and K^+ intercalated MXenes. (b) Corresponding normalized QENS (normalized and truncated for clarity) spectra at a representative $Q = 1.5 \text{ \AA}^{-1}$ (c) Dependence of the width of the QENS signal with Q^2 along with the diffusion coefficients of confined water evaluated from a jump model fit. Copyright 2017 American Chemical Society.

observation, they concluded that water in the $\text{Ti}_3\text{C}_2\text{T}_x$ MXene resides not between the layers, but instead in the inter stack gaps (Fig. 18 c). However, the elastic neutron scattering intensity does not show any steps when measured as a function of temperature, thus suggesting that the water in the inter stack gaps is still relatively strongly confined (Fig. 19, inset I). Furthermore, this water exhibits a diffusivity at ca. 50 % of the bulk water diffusivity, as demonstrated by QENS measurements (Fig. 19 and inset II). Their studies have also shown an increase in the *c*-L parameter after the metal ion (K^+) intercalation, where the metal ions hold the water tightly (hence, two order of magnitude decrease in water diffusivity as observed by QENS) between the layers. However, in $\text{Ti}_3\text{C}_2\text{T}_x$ MXene, synthesized using a mixture of LiCl and 10% HF, Muckely *et al.*¹⁵⁵ found water residing between the layers (Fig. 20 a, elastic scan showed no sign of bulk water), with its diffusivity dropped by two order of magnitude (Fig. 20 b and c) compared to the value reported for the 48% HF etched MXene. More interestingly, they reported a higher diffusivity of water (Fig. 20 c in the MXene intercalated with Mg^{2+} ions, which form a stronger hydration bonding compared to K^+). Based on this result, they concluded that it is the *d*-spacing, i.e., the structure the MXene, rather than the character of the ion-water bonding, that determines the mobility of water confined between the MXene layers. Additionally, Osti *et al.*¹⁵⁶ performed elastic and inelastic neutron scattering studies of annealed $\text{Ti}_3\text{C}_2\text{T}_x$ MXene. They showed the presence of hydrogen trapped in the MXenes, as evident from the step III in the elastic intensity scan (Fig. 21 a), that were synthesized using 48% HF to etch their parent MAX phases. This study was concerned with possible use of MXene in hydrogen storage and hydrogen evolution reaction catalysis. Their study further highlighted the fact that the milder etchant (Fig. 21 b), higher temperatures ($\sim 200 \text{ }^\circ\text{C}$), and metal ions intercalation all produce MXenes without trapped hydrogen. Furthermore, Osti *et al.*¹⁵⁷ investigated the vibrational dynamics of water confined between MXene layers together

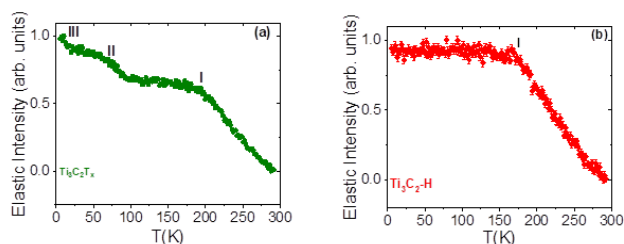


Fig. 21. Elastic neutron scattering intensities from two different MXenes synthesized using (a) 48% HF, (b) A mixture of 10% HF + LiCl. Both samples were annealed at 110°C to remove surface bound water before the measurements. Reprinted figures with permission from Phys. Rev. Mater 1, 024004 (2017). Copyright 2017 by the American Physical Society.

with metal ions using INS (Fig. 22) and MD simulations. INS spectra showed all the vibrational bands characteristic of water molecules, such as intermolecular translational modes (0–40 meV, Fig. 22 a), librational modes (40–140 meV, Fig. 22 b), intramolecular H-O-H bending (~ 205 meV, Fig. 22 c), and O-H stretching modes (400–450 meV, Fig. 22 d). However, compared to pristine MXene, they found a very small amount of water in metal ions (Li, Na and K) intercalated MXenes, where the water molecules were found to be more ordered. They reported an increasing trend on the ordering of the water molecules as the size of the ion is increased, which was further supported by the ion size dependent interference of water molecules observed in MD simulations.

Similar to carbon-based supercapacitor systems, performance of MXenes in electrochemical energy storage applications depends on the types of the electrolyte used. With a goal of increasing the energy and power density of MXene based supercapacitors, application of ionic liquids as electrolytes has recently started. Dall'Agnese *et al.*¹⁵⁸ measured the electrochemical performances of Ti_3C_2 MXene using 1 M solution of EmimTFSI in acetonitrile and then compared the results with 1 M solutions of EmimBF₄ and TEABF₄ (tetraethylammonium tetrafluoroborate). They demonstrated an increase in capacitance with a good electrochemical stability of $\text{Ti}_3\text{C}_2\text{T}_x$ MXene in the 1 M solution of EmimTFSI due to the simultaneous intercalation and deintercalation of Emim⁺ between the MXene layers during cycling through the electrodes. Moreover, they also found an increase in capacitance while using MXene-carbon nanotube composites as electrodes due to the high charge filtration of the electrodes. Later on, Jackel *et al.*¹⁴⁹ discovered that the $\text{Ti}_3\text{C}_2\text{T}_x$ MXene, even in the absence of external voltage, undergoes spontaneous cation intercalation when it comes in contact with ionic liquids, but the number of intercalated cations increases upon applying a negative potential. They further observed that the application of a positive voltage contracts the MXene electrodes significantly, leading to a thickness smaller than that at zero applied potential. A similar type of $\text{Ti}_3\text{C}_2\text{T}_x$ MXene electrodes expansion and contraction in EmimTFSI ionic liquid electrolytes has been reported in MD simulation.¹⁵⁹

In all the MXene-electrolyte systems that we have discussed above, ionic liquids are mixed with organic solvents and used as electrolytes. Lin *et al.*¹⁶⁰ for the first time used an ionic liquid, EmimTFSI as electrolyte and ionogel MXene as electrode (prepared by exchanging EmimTFSI with acetone and water),

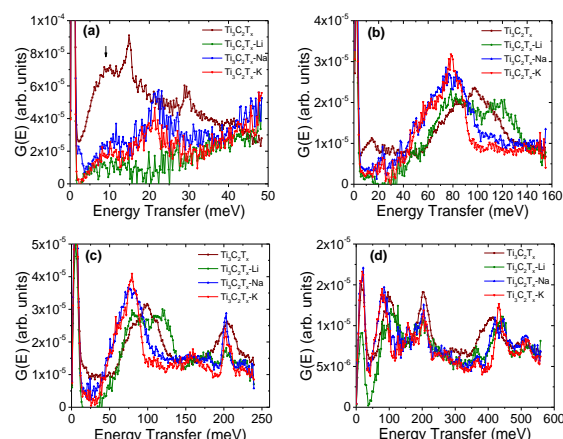


Fig. 22. A comparison of generalized vibrational density of states, $G(E)$ of pristine and metal ions (Li⁺, Na⁺ and K⁺) intercalated MXene measured at four neutron incident energies (a) $E_i = 50$ meV (b) $E_i = 160$ meV (c) $E_i = 250$ meV and (d) $E_i = 600$ meV at $T = 7$ K. Reprinted figures with permission from Phys. Rev. Mater 1, 065406 (2017). Copyright 2017 by the American Physical Society.

and investigated their electrochemical performances in a supercapacitor setup. They reported a higher gravimetric capacitance of 70 F g^{-1} from the MXene ionogel electrodes compared to 1 F g^{-1} from the dried $\text{Ti}_3\text{C}_2\text{T}_x$ MXene, even at high scan rate of 20 mV S^{-1} within the operational potential window of 3 V due to the insertion of ions (cations and anion) between the MXene layers. They observed a capacitance of $\sim 53 \text{ F g}^{-1}$ at even higher scan rate of 50 mV S^{-1} , indicating a higher power handling capability of the MXene ionogel electrodes.

In most MXene-electrolyte based systems, charge storing mechanisms are related to the solvent assisted intercalation of ions between the MXene layers, leading to an increase in d-spacing during cycling. Optimization of electrochemical performances of MXene-based systems is attempted by using either different MXene electrodes, or different types of the electrolytes. Wang *et al.*⁸⁹ investigated the influence of the solvents of an electrolyte on the charge storing capability of Ti_3C_2 MXene (synthesized by etching MAX phase by a mixture of HCl + LiF) using electrochemical measurements, MD simulations, and QENS techniques. They observed different arrangements of ions in the Ti_3C_2 MXene based on the chemical nature of the electrolyte solvents. They reported that the MXene doubled the charge storage when an electrolyte comprised of a mixture of propylene carbonate (PC) and lithium bis(trifluoromethylsulfonyl)amine (LiTFSI) was used. They found the presence of completely desolvated Li ions in the small interlayer spacing ($< 2.9 \text{ \AA}$) of Ti_3C_2 MXene in the PC/LiTFSI electrolyte system. Bulk-like behavior observed from the PC solvent in the QENS measurements further affirms the notion that PC does not enter in between the MXene layers but facilitates the intercalation/deintercalation of Li ions upon charging/discharging of the electrodes. They highlighted complete absence of solvent-ion interaction and fluid-solid interface formation between the MXene and the PC+LiTFSI electrolyte system.

Electrochemical behavior of MXene-ionic liquid systems for energy storage applications depends on the amount of charged species, as well as their mobilities within the MXene electrodes. With an aim of understanding the microscopic dynamics of ions

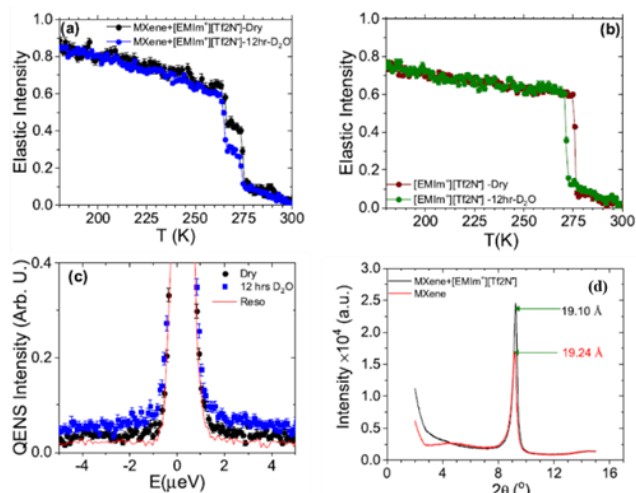


Fig. 23. A comparison of normalized elastic scan profiles (a) from dry and D₂O exposed [EMim+][Tf₂N⁻] confined MXene and (b) from bulk [EMim+][Tf₂N⁻]. (c) Normalized QENS spectra along with a resolution function collected from dry and D₂O exposed [EMim+][Tf₂N⁻] confined MXene. Data have been truncated both in x and y-axis for better visualization, (d) X-ray diffraction patterns of pristine and [EMim+][Tf₂N⁻] confined Ti₃C₂T_x MXene at two different states. Reprinted with permission from J. Phys. Chem. C 2018, 122, 27561–27566. Copyright 2018 American Chemical Society.

and correlating the ions mobilities with electrochemical performance, Osti *et al.*¹⁶¹ investigated the dynamics of EmimTFSI confined in the Ti₃C₂T_x MXene and explored the impact of humidity on the ion mobility using QENS and MD simulations for the first time. Elastic neutron scattering showed the presence of a two-step melting transition (Fig. 23 a), one from bulk-like ionic liquid and another from confined ionic liquid, as opposed to one step transition observed in bulk ionic liquid (Fig. 23 b). However, they reported a very small impact of water exposure on the ionic liquid confined in MXene compared to the bulk ionic liquid. The representative QENS spectra (Fig 23 c) from D₂O vapor exposed sample is broader compared to the dry sample, indicating an enhancement on cation mobility upon humidity exposure. The model based analysis of QENS spectra of MXene + EmimTFSI yielded a diffusion coefficient at roughly half $((0.42 \pm 0.08) \times 10^{-10} \text{m}^2 \text{s}^{-1})$ of the bulk value $((0.92 \pm 0.12) \times 10^{-10} \text{m}^2 \text{s}^{-1})$, similar to the situation observed for water in MXene¹⁵⁴, suggesting that the ionic liquid is not in between the layers. This is because one would expect a much more pronounced reduction in diffusivities for the truly nano-confined fluids compared to their bulk values.^{53, 154} Furthermore, XRD patterns collected before and after the EmimTFSI intercalation into the MXene gave almost the same d-spacing (Fig 23 d), confirming that the ionic liquid indeed resides in the MXene inter-stack gaps, and not between the layers. Exposure to D₂O vapor increases the mobility of the cations due to the displacement of the ions from the MXene surface, as demonstrated by the MD simulation, which shows an accumulation of water molecules on the MXene surface.

To summarize the results of QENS studies of intercalated species in MXenes, they share many similarities with studies of RTILs confined in carbon-based materials, but with an additional complication due to the more challenging morphology of many MXene samples featuring both inter-layer and inter-stack space. The latter don't affect the c-lattice parameter and thus cannot be inferred from diffraction studies, yet they may be

comparable in volume to, or even dominate over, the inter-layer space. This complex morphology of many MXene samples may offer both challenges and opportunities for energy storage applications.

Summary and outlook

Today's emerging energy crisis and increasing reliance on the renewable energy sources have dramatically impacted and reshaped energy storage research. Electrochemical capacitors, which store energy either by adsorption of the ions or by the redox reaction that takes place on the surface of the electrodes, are on the forefront of the energy storage research due to the opportunities they offer to optimize the performance by tuning the properties of both the electrodes and electrolytes. In EDLCs, increasing of the specific surface area of the electrodes and operational voltage window of electrolytes has been practiced to enhance the capacitance and the rate handling capabilities. This review mainly focuses on porous carbon and carbide derived electrodes and ionic liquids as electrolytes, which form complex interfaces. Carbons with uniform pores that match the size of the ions are found to have a larger capacitance. Nanoporous carbon electrodes with an ionic liquid as an electrolyte exhibit better energy and power density. More interestingly, in nano-confined systems, microscopic dynamics of electrolyte molecules is found to play a major role in controlling the device performance. We have presented many cases where QENS has been employed to explore the charge storing mechanisms based on the molecular level information on the complex structure and dynamics present at solid-electrolyte interfaces. The unique ability of QENS to probe hydrogen-bearing species (cations of ionic liquids) even in the presence of a heavy confining matrix provides a powerful tool to investigate the charged species attached to the pore walls, which are responsible for controlling the capacitance of the supercapacitors. Higher rate handling capability observed in porous electrodes-ionic liquids supercapacitors has been rationalized based on the higher diffusivity of the ions in pores away from the walls, as observed in the QENS measurements. The impact of humidity on the immobilization of charges on the electrode walls, which influences the electrochemical performance, can be readily studied by QENS using exposure of the electrode-electrolyte system to D₂O vapor, since deuterium incoherent and total neutron scattering cross-sections are much smaller compared to those of hydrogen. Likewise, the use of selectively deuterated co-solvents enables mobility studies of the specific electrolyte components, which is an added advantage of QENS. Similarly, the modifications of the ions layering on the surface of the electrodes under applied potential can be readily explored through monitoring the changes of the elastic scattering intensity obtained from QENS. Energy storage research is expanding quickly with the addition of new electrodes and electrolytes. A new family of MXene materials is an outstanding example of the rapid development on the forefront of the materials research for energy storage applications. Combinations of those novel electrodes and electrolytes in device configurations result in a formation of a

very complex interface, where understanding of the molecular-level structure and dynamics becomes non-trivial. Immobilization of ions on the electrode surfaces and the packing of the remaining ions in the middle of the pores are two important phenomena underlying performance of a supercapacitors. The basic properties of neutrons that we have discussed in this review make it possible to obtain a detailed information on the interfaces, even when they are hidden, thus enabling their development and modification to obtain supercapacitors of high power and energy density.

Conflicts of interest

There are no conflicts to declare.

Acknowledgements

The authors acknowledge support from the Fluid Interface Reactions, Structures and Transport (FIRST) Center, an Energy Frontier Research Center funded by the U.S. Department of Energy, Office of Science, Office of Basic Energy Sciences. Work at ORNL's Spallation Neutron Source is supported by the U.S. Department of Energy, Office of Basic Energy Sciences. Oak Ridge National Laboratory is managed by UT-Battelle, LLC, for U.S. DOE under Contract No. DEAC05-00OR22725.

Notes and references

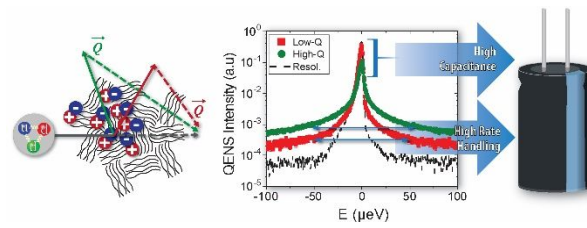
- 1 M. Aneke and M. H. Wang, *Appl. Energy*, 2016, **179**, 350-377.
- 2 T. M. I. Mahlia, T. J. Saktisandan, A. Jannifar, M. H. Hasan and H. S. C. Matseelar, *Renewable Sustainable Energy Rev.*, 2014, **33**, 532-545.
- 3 T. M. Gur, *Energy Environ. Sci.*, 2018, **11**, 2696-2767.
- 4 J. M. Tarascon and M. Armand, *Nature*, 2001, **414**, 359-367.
- 5 J. B. Goodenough and Y. Kim, *Chem. Mater.*, 2010, **22**, 587-603.
- 6 N. Yabuuchi, K. Kubota, M. Dahbi and S. Komaba, *Chem. Rev.*, 2014, **114**, 11636-11682.
- 7 N. S. Choi, Z. H. Chen, S. A. Freunberger, X. L. Ji, Y. K. Sun, K. Amine, G. Yushin, L. F. Nazar, J. Cho and P. G. Bruce, *Angew. Chem., Int. Ed.*, 2012, **51**, 9994-10024.
- 8 L. G. Lu, X. B. Han, J. Q. Li, J. F. Hua and M. G. Ouyang, *J. Power Sources*, 2013, **226**, 272-288.
- 9 A. Kraytsberg and Y. Ein-Eli, *J. Power Sources*, 2011, **196**, 886-893.
- 10 H. X. Ji, X. Zhao, Z. H. Qiao, J. Jung, Y. W. Zhu, Y. L. Lu, L. L. Zhang, A. H. MacDonald and R. S. Ruoff, *Nat. Commun.*, 2014, **5**, 3317-7.
- 11 L. Wei and G. Yushin, *Nano Energy*, 2012, **1**, 552-565.
- 12 P. Simon and Y. Gogotsi, *Nat. Mater.*, 2008, **7**, 845-854.
- 13 P. Simon, Y. Gogotsi and B. Dunn, *Science*, 2014, **343**, 1210-1211.
- 14 P. Simon and Y. Gogotsi, *Acc. Chem. Res.*, 2013, **46**, 1094-1103.
- 15 A. S. Arico, P. Bruce, B. Scrosati, J. M. Tarascon and W. Van Schalkwijk, *Nat. Mater.*, 2005, **4**, 366-377.
- 16 L. L. Zhang and X. S. Zhao, *Chem. Soc. Rev.*, 2009, **38**, 2520-2531.
- 17 Z. N. Yu, L. Tetard, L. Zhai and J. Thomas, *Energy Environ. Sci.*, 2015, **8**, 702-730.
- 18 F. Beguin, V. Presser, A. Balducci and E. Frackowiak, *Adv. Mater.*, 2014, **26**, 2219-2251.
- 19 A. G. Pandolfo and A. F. Hollenkamp, *J. Power Sources*, 2006, **157**, 11-27.
- 20 Q. F. Zhang, E. Uchaker, S. L. Candelaria and G. Z. Cao, *Chem. Soc. Rev.*, 2013, **42**, 3127-3171.
- 21 C. Zhong, Y. D. Deng, W. B. Hu, J. L. Qiao, L. Zhang and J. J. Zhang, *Chem. Soc. Rev.*, 2015, **44**, 7484-7539.
- 22 M. Salanne, *Top. Curr. Chem.*, 2017, **375**, 63-25.
- 23 A. Janes and E. Lust, *Electrochem. Commun.*, 2005, **7**, 510-514.
- 24 S. Boukhalifa, D. Gordon, L. L. He, Y. B. Melnichenko, N. Nitta, A. Magasinski and G. Yushin, *Acs Nano*, 2014, **8**, 2495-2503.
- 25 J. M. Griffin, A. C. Forse, W. Y. Tsai, P. L. Taberna, P. Simon and C. P. Grey, *Nat. Mater.*, 2015, **14**, 812-819.
- 26 M. Jayalakshmi and K. Balasubramanian, *Int. J. Electrochem. Sci.*, 2008, **3**, 1196-1217.
- 27 A. C. Forse, C. Merlet, J. M. Griffin and C. P. Grey, *J. Am. Chem. Soc.*, 2016, **138**, 5731-5744.
- 28 F. Blanc, M. Leskes and C. P. Grey, *Acc. Chem. Res.*, 2013, **46**, 1952-1963.
- 29 C. Zhan, C. Lian, Y. Zhang, M. W. Thompson, Y. Xie, J. Z. Wu, P. R. C. Kent, P. T. Cummings, D. E. Jiang and D. J. Wesolowski, *Adv. Sci.*, 2017, **4**, 1700059-27.
- 30 Z. Bo, C. W. Li, H. C. Yang, K. Ostrikov, J. H. Yan and K. F. Cen, *Nano-Micro Lett.*, 2018, **10**, 33-23.
- 31 M. Armand and J. M. Tarascon, *Nature*, 2008, **451**, 652-657.
- 32 Y. Wu and C. B. Cao, *Sci. China-Mater.*, 2018, **61**, 1517-1526.
- 33 C. F. Liu, Y. C. Liu, T. Y. Yi and C. C. Hu, *Carbon*, 2019, **145**, 529-548.
- 34 X. Li and B. Q. Wei, *Nano Energy*, 2013, **2**, 159-173.
- 35 G. P. Wang, L. Zhang and J. J. Zhang, *Chem. Soc. Rev.*, 2012, **41**, 797-828.
- 36 Y. W. Zhu, S. Murali, M. D. Stoller, K. J. Ganesh, W. W. Cai, P. J. Ferreira, A. Pirkle, R. M. Wallace, K. A. Cychoz, M. Thommes, D. Su, E. A. Stach and R. S. Ruoff, *Science*, 2011, **332**, 1537-1541.
- 37 H. Jiang, P. S. Lee and C. Z. Li, *Energy Environ. Sci.*, 2013, **6**, 41-53.
- 38 Q. Wang, J. Yan and Z. J. Fan, *Energy Environ. Sci.*, 2016, **9**, 729-762.
- 39 K. Jurewicz, C. Vix-Guterl, E. Frackowiak, S. Saadallah, A. Reda, J. Parmentier, J. Patarin and F. Beguin, *J. Phys. Chem. Solids*, 2004, **65**, 287-293.
- 40 J. A. Fernandez, T. Morishita, M. Toyoda, M. Inagaki, F. Stoeckli and T. A. Centeno, *J. Power Sources*, 2008, **175**, 675-679.
- 41 D. R. MacFarlane, N. Tachikawa, M. Forsyth, J. M. Pringle, P. C. Howlett, G. D. Elliott, J. H. Davis, M. Watanabe, P. Simon and C. A. Angell, *Energy Environ. Sci.*, 2014, **7**, 232-250.
- 42 S. J. Zhang, J. Sun, X. C. Zhang, J. Y. Xin, Q. Q. Miao and J. J. Wang, *Chem. Soc. Rev.*, 2014, **43**, 7838-7869.
- 43 M. Galinski, A. Lewandowski and I. Stepniak, *Electrochim. Acta*, 2006, **51**, 5567-5580.
- 44 M. Toupin, T. Brousse and D. Belanger, *Chem. Mater.*, 2004, **16**, 3184-3190.
- 45 M. G. Sullivan, B. Schnyder, M. Bartsch, D. Alliata, C. Barbero, R. Imhof and R. Kotz, *J. Electrochem. Soc.*, 2000, **147**, 2636-2643.
- 46 H. Wang, T. K. J. Koster, N. M. Trease, J. Segalini, P. L. Taberna, P. Simon, Y. Gogotsi and C. P. Grey, *J. Am. Chem.*

- Soc.*, 2011, **133**, 19270-19273.
- 47 L. Borchardt, M. Oschatz, S. Paasch, S. Kaskel and E. Brunner, *PCCP*, 2013, **15**, 15177-15184.
- 48 H. Wang, A. C. Forse, J. M. Griffin, N. M. Trease, L. Trognko, P. L. Taberna, P. Simon and C. P. Grey, *J. Am. Chem. Soc.*, 2013, **135**, 18968-18980.
- 49 G. A. Feng, R. Qiao, J. S. Huang, S. Dai, B. G. Sumpter and V. Meunier, *PCCP*, 2011, **13**, 1152-1161.
- 50 A. Gallegos, C. Lian, B. Dyatkin and J. Z. Wu, *Mol. Phys.*, 2019, **0026-8976**, 1-11.
- 51 Y. Shim and H. J. Kim, *ACS Nano*, 2010, **4**, 2345-2355.
- 52 Y. Shim, Y. Jung and H. J. Kim, *J. Phys. Chem. C*, 2011, **115**, 23574-23583.
- 53 N. C. Osti, A. Cote, E. Mamontov, A. Ramirez-Cuesta, D. J. Wesolowski and S. O. Diallo, *Chem. Phys.*, 2016, **465**, 1-8.
- 54 J. S. Higgins, *Annu. Rev. Chem. Biomol. Eng.*, **7**, pp. 1-18.
- 55 J. F. Li, T. Ngai and C. Wu, *Polym. J.*, 2010, **42**, 609-625.
- 56 N. C. Osti, T. N. Etampawala, U. M. Shrestha, D. Aryal, M. Tyagi, S. O. Diallo, E. Mamontov, C. J. Cornelius and D. Perahia, *J. Chem. Phys.*, 2016, **145**, 224902-9.
- 57 N. C. Osti, E. Mamontov, L. Daemen, J. F. Browning, J. Keum, H. C. Ho, J. H. Chen, K. L. Hong and S. O. Diallo, *J. Appl. Polym. Sci.*, 2019, **136**, 47394-9.
- 58 D. Vural, X. H. Hu, B. Lindner, N. Jain, Y. L. Miao, X. L. Cheng, Z. Liu, L. Hong and J. C. Smith, *Biochim. Biophys. Acta-Gen. Subj.*, 2017, **1861**, 3638-3650.
- 59 S. Mitra and R. Mukhopadhyay, *Pramana-Journal of Physics*, 2004, **63**, 81-89.
- 60 T. Heitmann, G. Hester, S. Mitra, T. Calloway, M. S. Tyagi, A. Miskowicz, S. Diallo, N. Osti and E. Mamontov, *Solid State Ionics*, 2019, **334**, 95-98.
- 61 M. Bee, *Quasielastic Neutron Scattering: Principles and Applications in Solid State Chemistry, Biology, and Materials Science*, Adam Hilger, Bristol, 1998.
- 62 E. Mamontov, R. W. Smith, J. J. Billings and A. J. Ramirez-Cuesta, *Phys. B.*, 2019, **566**, 50-54.
- 63 E. Mamontov, H. M. Luo and S. Dai, *J. Phys. Chem. B*, 2009, **113**, 159-169.
- 64 Z. D. Deng and K. A. Mauritz, *Macromolecules*, 1992, **25**, 2739-2745.
- 65 D. L. Price, O. Borodin, M. Gonzalez, M. Kofu, K. Shibata, T. Yamada, O. Yamamuro and M. L. Saboungi, *J. Phys. Chem. Lett.*, 2017, **8**, 715-719.
- 66 A. Triolo, O. Russina, B. Fazio, R. Triolo and E. Di Cola, *Chem. Phys. Lett.*, 2008, **457**, 362-365.
- 67 R. Hayes, G. G. Warr and R. Atkin, *Chem. Rev.*, 2015, **115**, 6357-6426.
- 68 T. Murphy, R. Atkin and G. G. Warr, *Curr. Opin. Colloid Interface Sci.*, 2015, **20**, 282-292.
- 69 J. N. C. Lopes and A. A. H. Padua, *J. Phys. Chem. B*, 2006, **110**, 19586-19592.
- 70 J. Lopes and A. A. H. Padua, *J. Phys. Chem. B*, 2006, **110**, 3330-3335.
- 71 J. N. C. Lopes and A. A. H. Padua, *J. Phys. Chem. B*, 2004, **108**, 16893-16898.
- 72 K. Shimizu, M. F. C. Gomes, A. A. H. Padua, L. P. N. Rebelo and J. N. C. Lopes, *J. Mol. Struct.: THEOCHEM*, 2010, **946**, 70-76.
- 73 H. Weingaertner, *Angew. Chem., Int. Ed.*, 2008, **47**, 654-670.
- 74 H. Tokuda, K. Hayamizu, K. Ishii, M. Susan and M. Watanabe, *J. Phys. Chem. B*, 2005, **109**, 6103-6110.
- 75 P. Yee, J. K. Shah and E. J. Maginn, *J. Phys. Chem. B*, 2013, **117**, 12556-12566.
- 76 A. Triolo, O. Russina, V. Arrighi, F. Juranyi, S. Janssen and C. M. Gordon, *J. Chem. Phys.*, 2003, **119**, 8549-8557.
- 77 M. C. C. Ribeiro, *J. Phys. Chem. B*, 2007, **111**, 5008-5015.
- 78 Y. Inamura, O. Yamamuro, S. Hayashi and H. O. Hamaguchi, *Phys. B*, 2006, **385**, 732-734.
- 79 E. Mamontov, G. A. Baker, H. Luo and S. Dai, *Chemphyschem*, 2011, **12**, 944-950.
- 80 B. Aoun, M. A. Gonzalez, J. Ollivier, M. Russina, Z. Izaola, D. L. Price and M. L. Saboungi, *J. Phys. Chem. Lett.*, 2010, **1**, 2503-2507.
- 81 O. Yamamuro, T. Yamada, M. Kofu, M. Nakakoshi and M. Nagao, *J. Chem. Phys.*, 2011, **135**, 054508-7.
- 82 J. P. Embs, T. Burankova, E. Reichert and R. Hempelmann, *J. Phys. Chem. B*, 2012, **116**, 13265-13271.
- 83 T. Burankova, E. Reichert, V. Fossog, R. Hempelmann and J. P. Embs, *J. Mol. Liq.*, 2014, **192**, 199-207.
- 84 T. Burankova, R. Hempelmann, A. Wildes and J. P. Embs, *J. Phys. Chem. B*, 2014, **118**, 14452-14460.
- 85 T. Burankova, R. Hempelmann, V. Fossog, J. Ollivier, T. Seydel and J. P. Embs, *J. Phys. Chem. B*, 2015, **119**, 10643-10651.
- 86 T. Burankova, G. Simeoni, R. Hempelmann, J. F. M. Cardozo and J. P. Embs, *J. Phys. Chem. B*, 2017, **121**, 240-249.
- 87 M. Kofu, M. Tyagi, Y. Inamura, K. Miyazaki and O. Yamamuro, *J. Chem. Phys.*, 2015, **143**, 234502-10.
- 88 P. Dhakal and J. K. Shah, *Journal*, 2019, **18**, 90-97.
- 89 X. Wang, T. S. Mathis, K. Li, Z. Lin, L. Vlcek, T. Torita, N. C. Osti, C. Hatter, P. Urbankowski, A. Sarycheva, M. Tyagi, E. Mamontov, P. Simon and Y. Gogotsi, *Nat. Energy*, 2019, **4**, 241-248.
- 90 K. Van Aken, M. Beidaghi and Y. Gogotsi, *Angew. Chem.*, 2015, **127**, 1-5.
- 91 K. Liu and J. Z. Wu, *J. Phys. Chem. C*, 2016, **120**, 24041-24047.
- 92 K. Liu, C. Lian, D. Henderson and J. Z. Wu, *Mol. Phys.*, 2017, **115**, 454-464.
- 93 N. C. Osti, K. L. Van Aken, M. W. Thompson, F. Tiet, D. E. Jiang, P. T. Cummings, Y. Gogotsi and E. Mamontov, *J. Phys. Chem. Lett.*, 2017, **8**, 167-171.
- 94 M. W. Thompson, R. Matsumoto, R. L. Sacci, N. C. Sanders and P. T. Cummings, *J. Phys. Chem. B*, 2019, **123**, 1340-1347.
- 95 N. C. Osti, R. A. Matsumoto, M. W. Thompson, P. T. Cummings, M. Tyagi and E. Mamontov, *J. Phys. Chem. C*, 2019, **123**, 19354-19361.
- 96 J. Qvist, H. Schober and B. Halle, *J. Chem. Phys.*, 2011, **134**.
- 97 E. Mamontov, *Chem. Phys. Lett.*, 2012, **530**, 55-60.
- 98 O. Borodin and G. D. Smith, *J. Phys. Chem. B*, 2006, **110**, 11481-11490.
- 99 O. Borodin, W. Gorecki, G. D. Smith and M. Armand, *J. Phys. Chem. B*, 2010, **114**, 6786-6798.
- 100 D. W. Wang, F. Li, M. Liu, G. Q. Lu and H. M. Cheng, *J. Phys. Chem. C*, 2008, **112**, 9950-9955.
- 101 H. Wang, Z. W. Xu, A. Kohandehghan, Z. Li, K. Cui, X. H. Tan, T. J. Stephenson, C. K. King'ondeu, C. M. B. Holt, B. C. Olsen, J. K. Tak, D. Harfield, A. O. Anyia and D. Mitlin, *ACS Nano*, 2013, **7**, 5131-5141.
- 102 X. M. Fan, C. Yu, J. Yang, Z. Ling, C. Hu, M. D. Zhang and J. S. Qiu, *Adv. Energy Mater.*, 2015, **5**, 1401761-7.
- 103 S. M. Chathoth, E. Mamontov, S. Dai, X. Wang, P. F. Fulvio and D. J. Wesolowski, *Epl*, 2012, **97**, 66004-6.
- 104 E. Mamontov and K. W. Herwig, *Rev. Sci. Instrum.*, 2011, **82**, 284104-10.
- 105 C. Pinilla, M. G. Del Popolo, R. M. Lynden-Bell and J.

- Kohanoff, *J. Phys. Chem. B*, 2005, **109**, 17922-17927.
- 106 S. M. Chathoth, E. Mamontov, P. F. Fulvio, X. Wang, G. A. Baker, S. Dai and D. J. Wesolowski, *Epl*, 2013, **102**, 16004-p5.
- 107 K. L. Van Aken, J. K. McDonough, S. Li, G. Feng, S. M. Chathoth, E. Mamontov, P. F. Fulvio, P. T. Cummings, S. Dai and Y. Gogotsi, *J. Phys.: Condens. Matter*, 2014, **26**, 284104-10.
- 108 V. L. Kuznetsov, A. L. Chuvilin, Y. V. Butenko, I. Y. Malkov and V. M. Titov, *Chem. Phys. Lett.*, 1994, **222**, 343-348.
- 109 G. Feng, S. Li, V. Presser and P. T. Cummings, *J. Phys. Chem. Lett.*, 2013, **4**, 3367-3376.
- 110 J. L. Banelos, G. Feng, P. F. Fulvio, S. Li, G. Rother, S. Dai, P. T. Cummings and D. J. Wesolowski, *Chem. Mater.*, 2014, **26**, 1144-1153.
- 111 B. Dyatkin, E. Mamontov, K. M. Cook and Y. Gogotsi, *Prog. Nat. Sci.: Mater. Int.*, 2015, **25**, 631-641.
- 112 B. Dyatkin, Y. Zhang, E. Mamontov, A. I. Kolesnikov, Y. Q. Cheng, H. M. Meyer, P. T. Cummings and Y. Gogotsi, *J. Phys. Chem. C*, 2016, **120**, 8730-8741.
- 113 M. Rouha and P. T. Cummings, *PCCP*, 2015, **17**, 4152-4159.
- 114 R. Futamura, T. Iiyama, Y. Takasaki, Y. Gogotsi, M. J. Biggs, M. Salanne, J. Segalini, P. Simon and K. Kaneko, *Nat. Mater.*, 2017, **16**, 1225-+.
- 115 B. Dyatkin, N. C. Osti, Y. Zhang, H.-W. Wang, E. Mamontov, W. T. Heller, P. Zhang, G. Rother, P. T. Cummings, D. J. Wesolowski and Y. Gogotsi, *Carbon*, 2018, **129**, 104-118.
- 116 M. G. Montalban, C. L. Bolivar, F. G. D. Banos and G. Villora, *J. Chem. Eng. Data*, 2015, **60**, 1986-1996.
- 117 Y. Zhang and E. J. Maginn, *PCCP*, 2014, **16**, 13489-13499.
- 118 C. M. Gordon, J. D. Holbrey, A. R. Kennedy and K. R. Seddon, *J. Mater. Chem.*, 1998, **8**, 2627-2636.
- 119 B. Dyatkin, N. C. Osti, A. Gallegos, Y. Zhang, E. Mamontov, P. T. Cummings, J. Z. Wu and Y. Gogotsi, *Electrochim. Acta*, 2018, **283**, 882-893.
- 120 N. C. Osti, B. Dyatkin, A. Gallegos, D. Voneshen, J. K. Keum, K. Littrell, P. F. Zhang, S. Dai, J. Z. Wu, Y. Gogotsi and E. Mamontov, *J. Electrochem. Soc.*, 2019, **166**, A507-A514.
- 121 R. I. Bewley, J. W. Taylor and S. M. Bennington, *Nucl. Instrum. Methods Phys. Res., Sect. A*, 2011, **637**, 128-134.
- 122 A. L. Sturlaugson, K. S. Fruchey and M. D. Fayer, *J. Phys. Chem. B*, 2012, **116**, 1777-1787.
- 123 N. C. Osti, B. Dyatkin, M. W. Thompson, F. Tiet, P. F. Zhang, S. Dai, M. Tyagi, P. T. Cummings, Y. Gogotsi, D. J. Wesolowski and E. Mamontov, *Phys. Rev. Materials*, 2017, **1**, 035402-10.
- 124 S. Kazemiabnavi, Z. C. Zhang, K. Thornton and S. Banerjee, *J. Phys. Chem. B*, 2016, **120**, 5691-5702.
- 125 Z. Weng, F. Li, D. W. Wang, L. Wen and H. M. Cheng, *Angew. Chem., Int. Ed.*, 2013, **52**, 3722-3725.
- 126 R. Liu, J. Duay and S. B. Lee, *Chem. Commun.*, 2011, **47**, 1384-1404.
- 127 L. Demarconnay, E. Raymundo-Pinero and F. Beguin, *J. Power Sources*, 2011, **196**, 580-586.
- 128 S. Vaquero, J. Palma, M. Anderson and R. Marcilla, *J. Electrochem. Soc.*, 2013, **160**, A2064-A2069.
- 129 C. Lian, K. Liu, K. L. Van Aken, Y. Gogotsi, D. J. Wesolowski, H. L. Liu, D. E. Jiang and J. Z. Wu, *ACS Energy Lett.*, 2016, **1**, 21-26.
- 130 N. C. Osti, A. Gallegos, B. Dyatkin, J. Z. Wu, Y. Gogotsi and E. Mamontov, *J. Phys. Chem. C*, 2018, **122**, 10476-10481.
- 131 C. Lian, S. L. Zhao, H. L. Liu and J. Z. Wu, *J. Chem. Phys.*, 2016, **145**, 204707-6.
- 132 J. N. Neal, D. J. Wesolowski, D. Henderson and J. Z. Wu, *J. Chem. Phys.*, 2017, **146**, 174701-7.
- 133 S. M. Mahurin, E. Mamontov, M. W. Thompson, P. Zhang, C. H. Turner, P. T. Cummings and S. Dai, *Appl. Phys. Lett.*, 2016, **109**, 143111.
- 134 M. Mahurin, S. P. Surwade, M. Crespo and S. Dai, *J. Raman Spectrosc.*, 2016, **47**, 585-590.
- 135 E. Mamontov, S. M. Mahurin and S. Dai, *AIP Conf. Proc.* 2018, 1969, 020001-6.
- 136 M. Naguib, M. Kurtoglu, V. Presser, J. Lu, J. Niu, M. Heon, L. Hultman, Y. Gogotsi and M. W. Barsoum, *Adv. Mater.*, 2011, **23**, 4248-4253.
- 137 M. R. Lukatskaya, O. Mashtalir, C. E. Ren, Y. Dall'Agnese, P. Rozier, P. L. Taberna, M. Naguib, P. Simon, M. W. Barsoum and Y. Gogotsi, *Science*, 2013, **341**, 1502-1505.
- 138 O. Mashtalir, M. Naguib, V. N. Mochalin, Y. Dall'Agnese, M. Heon, M. W. Barsoum and Y. Gogotsi, *Nat. Commun.*, 2013, **4**, 1716-7.
- 139 O. Mashtalir, M. R. Lukatskaya, A. I. Kolesnikov, E. Raymundo-Pinero, M. Naguib, M. W. Barsoum and Y. Gogotsi, *Nanoscale*, 2016, **8**, 9128-9133.
- 140 M. Naguib, V. N. Mochalin, M. W. Barsoum and Y. Gogotsi, *Adv. Mater.*, 2014, **26**, 992-1005.
- 141 B. Anasori, M. Lukatskaya and Y. Gogotsi, *Nat. Rev. Mater.*, 2017, **2**, 16098-27.
- 142 M. Naguib and Y. Gogotsi, *Acc. Chem. Res.*, 2015, **48**, 128-135.
- 143 M. Khazaei, A. Ranjbar, M. Arai, T. Sasaki and S. Yunoki, *J. Phys. Chem. C*, 2017, **5**, 2488-2503.
- 144 V. M. H. Ng, H. Huang, K. Zhou, P. S. Lee, W. X. Que, J. Z. Xu and L. B. Kong, *J. Mater. Chem. A*, 2017, **5**, 3039-3068.
- 145 S. J. Sun, C. Liao, A. M. Hafez, H. L. Zhu and S. P. Wu, *Chem. Eng. J.*, 2018, **338**, 27-45.
- 146 C. Zhan, W. Sun, Y. Xie, D.-e. Jiang and R. P. Kent, *ACS Appl. Mater. Interfaces*, 2019, **11**, 24885-24905.
- 147 M. Okubo, A. Sugahara, S. Kajiyama and A. Yamada, *Acc. Chem. Res.*, 2018, **51**, 591-599.
- 148 D. P. Dubal, N. R. Chodankar, D. H. Kim and P. Gomez-Romero, *Chem. Soc. Rev.*, 2018, **47**, 2065-2129.
- 149 N. Jackel, B. Kruner, K. L. Van Aken, M. Alhabeb, B. Anasor, F. Kaasik, Y. Gogotsi and V. Presser, *ACS Appl. Mater. Interfaces*, 2016, **8**, 32089-32093.
- 150 X. Zhao, C. Dall'Agnese, X. F. Chu, S. S. Zhao, G. Chen, Y. Gogotsi, Y. Gao and Y. Dall'Agnese, *ChemSusChem*, 2019, **12**, 4516-4521.
- 151 Y. Xie, M. Naguib, V. N. Mochalin, M. W. Barsoum, Y. Gogotsi, X. Yu, K.-W. Nam, X.-Q. Yang, A. I. Kolesnikov and P. R. C. Kent, *J. Am. Chem. Soc.*, 2014, **136**, 6385-6394.
- 152 H.-W. Wang, M. Naguib, K. Page, D. J. Wesolowski and Y. Gogotsi, *Chem. Mater.*, 2016, **28**, 349-359.
- 153 S. H. Overbury, A. I. Kolesnikov, G. M. Brown, Z. Y. Zhang, G. S. Nair, R. L. Sacci, R. Lotfi, A. C. T. van Duin and M. Naguib, *J. Am. Chem. Soc.*, 2018, **140**, 10305-10314.
- 154 N. C. Osti, M. Naguib, A. Ostadhossein, Y. Xie, P. R. C. Kent, B. Dyatkin, G. Rother, W. T. Heller, A. C. T. van Duin, Y. Gogotsi and E. Mamontov, *ACS Appl. Mater. Interfaces*, 2016, **8**, 8859-8863.
- 155 E. S. Muckley, M. Naguib, H. W. Wang, L. Vlcek, N. C. Osti, R. L. Sacci, X. H. Sang, R. R. Unocic, Y. Xie, M. Tyagi, E. Mamontov, K. L. Page, P. R. C. Kent, J. Nanda and I. N. Ivanov, *ACS Nano*, 2017, **11**, 11118-11126.

- 156 N. C. Osti, M. Naguib, M. Tyagi, Y. Gogotsi, A. I. Kolesnikov and E. Mamontov, *Phys. Rev. Mater.* 2017, **1**, 024004-6.
- 157 N. C. Osti, M. Naguib, K. Ganeshan, Y. K. Shin, A. Ostadhossein, A. C. T. van Duin, Y. Q. Cheng, L. L. Daemen, Y. Gogotsi, E. Mamontov and A. I. Kolesnikov, *Phys. Rev. Mater.*, **1**, 065406-8.
- 158 Y. Dall'Agnese, P. Rozier, P. L. Taberna, Y. Gogotsi and P. Simon, *J. Power Sources*, 2016, **306**, 510-515.
- 159 K. Xu, Z. F. Lin, C. Merlet, P. L. Taberna, L. Miao, J. J. Jiang and P. Simon, *ChemSusChem*, 2018, **11**, 1892-1899.
- 160 Z. F. Lin, D. Barbara, P. L. Taberna, K. L. Van Aken, B. Anasori, Y. Gogotsi and P. Simon, *J. Power Sources*, 2016, **326**, 575-579.
- 161 N. C. Osti, M. W. Thompson, K. L. Van Aken, M. Alhabeab, M. Tyagi, J. K. Keum, P. T. Cummings, Y. Gogotsi and E. Mamontov, *J. Phys. Chem. C*, 2018, **122**, 27561-27566.

TOC Graphics



Quasielastic neutron scattering uniquely explores the mechanisms to achieve higher capacitance and rate handling in ionic liquids-based supercapacitor materials